

AD-A075 114

WEBB ASSOCIATES INC YELLOW SPRINGS OHIO  
THE PRECIPITATING ELECTRON DETECTORS (SSJ/3) FOR THE BLOCK 5D/F--ETC(U)  
AUG 79 M S GUSSENHOVEN , D A HARDY , A HUBER F49620-77-C-0050

F/G 4/1

UNCLASSIFIED

AFOSR-TR-79-1060

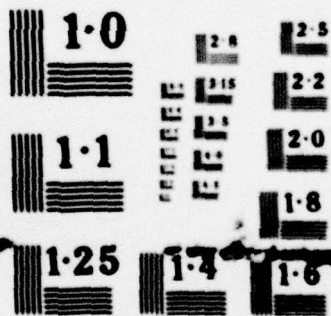
NL

1 OF 1  
AD-  
A075114



END  
DATE  
FILMED

11-79  
DDC



NATIONAL BUREAU OF STANDARDS  
MICROCOPY RESOLUTION TEST CHART

DA075114

DDC FILE COPY

18 AFOSR-TR-79-1060

LEVEL

DDC  
RECEIVED  
OCT 12 1979  
E

10

M. S. /Gussenhoven, D. A. /Hardy  
A. /Huber

6

THE PRECIPITATING ELECTRON DETECTORS (SSJ/3) FOR THE  
BLOCK 5D/ELIGHTS 2-5 DMSP SATELLITES:  
CALIBRATION AND DATA PRESENTATION.

12/64

11 Aug 79

16 2311

15 F49620-77-C-0050

17 AL

9 Final rept. 1 Jan 77-30 Sep 78

AIR FORCE OFFICE OF SCIENTIFIC RESEARCH (AFSC)  
NOTICE OF TRANSMITTAL TO DDC  
This technical report has been reviewed and is  
approved for public release IAW AFR 190-12 (7b).  
Distribution is unlimited.  
A. D. BLOSE  
Technical Information Officer

Approved for public release;  
distribution unlimited.

D.A.Hardy (Air Force Geophysics Lab, Hanscom AFB, MA)  
M.S.Gussenhoven (Boston College, Chestnut Hills, MA)  
A.Huber (Emmanuel College, The Fenway, Boston, MA)

JOB

401 286 79 10 12 026

REPORT DOCUMENTATION PAGE		READ INSTRUCTIONS BEFORE COMPLETING FORM
1. REPORT NUMBER <b>AFOSR-TR-79-1060</b>	2. GOVT ACCESSION NO.	3. RECIPIENT'S CATALOG NUMBER
4. TITLE (and Subtitle) <b>THE PRECIPITATING ELECTRON DETECTORS (SSJ/3) FOR THE BLOCK 5D/FLIGHTS 2-5 DMSP SATELLITES: CALIBRATION AND DATA PRESENTATION</b>		5. TYPE OF REPORT & PERIOD COVERED <b>01 Jan 77 - 30 Sep 78 Final (F000-11)</b>
7. AUTHOR(s) <b>M S Gussenhoven D A Hardy A Huber</b>		6. PERFORMING ORG. REPORT NUMBER
9. PERFORMING ORGANIZATION NAME AND ADDRESS <b>Webb Associates, Inc. Box 308 Yellow Springs, OH 45337</b>		8. CONTRACT OR GRANT NUMBER(s) <b>F49620-77-C-0050</b>
11. CONTROLLING OFFICE NAME AND ADDRESS <b>AFOSR /NP Bolling AFB Wash DC 20332</b>		10. PROGRAM ELEMENT, PROJECT, TASK AREA & WORK UNIT NUMBERS <b>61102F 2311/A1</b>
14. MONITORING AGENCY NAME & ADDRESS (if different from Controlling Office)		12. REPORT DATE <b>Aug 1979</b>
		13. NUMBER OF PAGES <b>62</b>
		15. SECURITY CLASS. (of this report) <b>unclassified</b>
		15a. DECLASSIFICATION/DOWNGRADING SCHEDULE
16. DISTRIBUTION STATEMENT (of this Report)  <i>Approved for public release; distribution unlimited.</i>		
17. DISTRIBUTION STATEMENT (of the abstract entered in Block 20, if different from Report)		
18. SUPPLEMENTARY NOTES		
19. KEY WORDS (Continue on reverse side if necessary and identify by block number)		
20. ABSTRACT (Continue on reverse side if necessary and identify by block number)  The work under this contract had as its goal the time-dependent phenomenological modeling of the polar cap regions. The vehicle for modeling the caps has been to analyze the following collection of data: DMSP images showing polar cap auroras; DMSP electron measurements; hourly averages of the interplanetary magnetic field; ground magnetometer data from Thule; and magnetic indices. DMSP images from the winters of 1972-1973 and 1974-1975 provided consistently good records of the northern polar cap region and were used as the primary		



basis of the study. The DMSP images for these periods were traced and gridded in corrected geomagnetic coordinates and local geomagnetic time. The subset of cases for which auroras occur at above 80 degrees corrected geomagnetic latitude was identified and further categorized by local time interval of occurrence (morning, midnight, evening sectors). The occurrence of extremely high latitude aurora in each category was correlated with magnetic indices, magnetometer response at Thule, and solar wind parameters. The correlation of cap size as determined by poleward auroral boundaries, and the time variation of these with the above parameters was also made.

79 10 12 026

UNCLASSIFIED

## ABSTRACT

In addition to weather monitoring devices, the DMSP satellites currently have on board auroral imaging devices, precipitating electron detectors, and thermal plasma analyzers. Together these provide a strong tool for analyzing the high latitude near Earth, magnetospheric environment. The Program is planned to continue into the 1980s.

The precipitating electrons are measured in 16 energy channels spanning an energy range of 50eV to 20keV. The data are routinely processed at the Air Force Geophysics Laboratories and have the potential of providing real-time monitoring of auroral activity through oval boundary measurements.

To facilitate the use of these data and to examine the feasibility of making consistent, reliable boundary measurements this report has been prepared. It contains the following: 1) A general description of the DMSP-F2 orbit, its variations in universal time and season, and the pertinence of these variations to boundary measurements. 2) A description of the SSJ/3 package, one of which is built for each of four DMSP satellites and the results of calibrating two of the instruments. 3) A discussion of the way the data is processed at the Air Force Geophysics Laboratories; 4) A comparison of Northpole - Southpole passes during a magnetospherically quiet period and during an active period, and a discussion of the general features of the electron precipitation as they may be used to determine auroral boundaries.

Acquisition for	WIC C-441
DOC TAB	
Announced	
Justification	
Y	
Distribution/	
Availability Code	
Avail and/or	
special	
st	A



## INTRODUCTION

The Defense Meteorological Satellite Program (DMSP) of the U.S. Air Force is now projected to continue well into the 1980s. The Program calls for two satellites to be in polar orbit at all times: one in the dawn-dusk meridian and one in the noon-midnight meridian. Depending on launch dates and system lifetimes there can be as many as three or as few as one satellite in operation at a given time. The Program is principally devoted to weather monitoring but radiometers operating over darkened areas produce the now familiar images of the auroral regions. These images provided the first extended views of auroral phenomena, and are available from 1971 to the present.

Since 1974, low-energy electron analyzers have been placed on dawn-dusk satellites in the Program. The satellites are non-spinning and the detectors are positioned to measure precipitating electrons. The original electrostatic analysers measured electrons in six channels from .2 to 20 keV. Since July, 1977, with the launch of DMSP-F2, these have been replaced by a set of two electrostatic analyzers on board covering the range 50 eV to 20 keV in 16 energy channels. An identical package was also flown on the F-3 satellite and additional instruments will be on DMSP F4 and F5 (dawn-dusk and noon-midnight orbits) which have yet to be launched. With DMSP F6, F7 and F8 additional electrostatic analyzers will be included to measure the flux of precipitating protons. Together with the imaging devices the improved measurements of precipitating electrons will continue to give this Program a central place in the continuing understanding of auroral and polar cap phenomena, and their relation to magnetospheric dynamics.

The spatial extent and small-scale resolution of the DMSP images has greatly increased the accuracy with which large numbers of researchers can visualize auroral activity. One now commonly makes reference to an "instantaneous" auroral

oval since large portions of the auroral zone can often be seen on a single DMSP image. Because of the considerable influence of the images on auroral research and because they continue to be routinely made, considerable effort has gone into the calibration of the sensitivity of the images to incorporate them accurately into the body of other past and future auroral measurements. (Mizera, et al, 1975; Mende and Eather, 1976; Eather, to be published). For similar reasons we have prepared this report on the current and projected precipitating electron measurements made by DMSP. These data are available in raw count form from the World Data Center. In addition, all the data is processed in the manner we report here at the Air Force Geophysics Laboratory.

It should also be noted that the auroral visual and particle data from DMSP may be supplemented with simultaneous measurements of the ionospheric thermal plasma by the SSIE instrument, (Smiddy, et al., 1978). This instrument was designed to measure the mass, density and temperature of the thermal ions as well as the density and temperature of the thermal electrons. Outputs are used by Air Weather Service to provide F region scale heights for global ionospheric modelling. Obviously, comparisons of simultaneous SSIE and SSJ/3 measurements can be exploited to provide unique information for modelling the dynamic response of the ionosphere to directly measured inputs from energetic particles.

The current measurements of precipitating electrons appear to be of such consistently high quality that their use to monitor the auroral regions on a real time basis is an obvious and important use of the data, particularly with the long time delay before A-indices are available. For this reason we will focus on the problems of obtaining consistent, meaningful auroral boundaries from the data. The quantity of data also makes possible accurate statistical surveys of particular features of auroral activity and their relation to



interplanetary and magnetospheric conditions. Earlier DMSP electron data has been used by Meng et al., (1977) and Meng and Kroehl (1977) to show correlations between the direction of the interplanetary magnetic field and differences in fluxes both between polar caps and dawn to dusk in a single cap. (See also the review by Mizera and Fennell (1978) for contributions from the Isis satellites).

Other detectors on spinning satellites have necessarily sacrificed time resolution for pitch angle distributions. DMSP satellites since they are non-spinning, have excellent time resolution, but no resolution in pitch angle. The DMSP satellite data can provide, therefore, an extension to the many interesting types of events recorded by other satellites, such as the intense keV fluxes in the caps reported by Foster and Burrows (1976) to occur after major storms. Additionally, any case study of events in the magnetosphere can have as an additional environmental input the state of the auroral and cap regions as determined by the DMSP images and the precipitating electrons.

This report, then, contains the following:

1. A general description of the DMSP-F2 orbit: the currently orbiting satellite.
2. A description of the SSJ/3 package, one of which is built for each of the F2, F3, F4, F5 satellites; and the results of calibrating the last two instruments. These calibrations are compared to the previous calibrations of the first two instruments.
3. A discussion of the way the data is processed at the Air Force Geophysics Laboratories.
4. A comparison of North pole-South pole passes during a magnetospherically quiet period and during an active period; and a discussion of the general features of the electron precipitation particularly for the purpose of determining auroral boundaries.

4

1. The DMSP-F2 Orbit.

DMSP-F2 was launched into a circular polar orbit in July, 1977. The orbit has an inclination of  $99^\circ$ , an altitude of 830 km and a period of 101 min. It is sun-synchronous and remains throughout its lifetime at the same inclination of  $9^\circ$  from the geographic poles and in the dawn to dusk plane. Since the magnetic poles rotate about the geographic poles, the F2 orbit changes systematically in geomagnetic coordinates throughout a 24-hour period.

Summaries of the satellite paths over the north and south polar regions throughout Day 59, 1978 (Feb 28) are given in Figures 1 and 2. The South polar plots are similar to those given by Candidi et al., (1978). The paths have been projected along magnetic field lines to 100 km using a Jensen-Cain model of the magnetic field; and the corrected geomagnetic latitudes of the projections are plotted as a function of magnetic local time. The paths are drawn across the magnetic latitude interval  $70^\circ$ - $90^\circ$  for both poles. Each line represents the path for the approximate UT listed at the side, starting at the beginning of the day. The areas of cross-hatching represent a group of paths for the time interval listed.

For a broad time interval ( ~ 0:00 - 11:00 UT) the subsatellite path falls across the polar cap in both polar regions, varying in geomagnetic local time from 1800 - 2100 at  $70^\circ$  in the evening (dusk), and 5:30 - 8:30 at  $70^\circ$  in the morning (dawn). For universal times greater than 11:00 UT the north polar satellite path will not reach geomagnetic latitudes greater than  $80^\circ$  and will lie at latitudes, for the most part, in the midnight sector "instantaneous" oval. The same is true for the south polar region except that satellite paths for times greater than 11:00 UT are in the midday sector at cusp latitudes and below.



The satellite orbits are constant in UT over the life of the satellite in geographic and, therefore, geomagnetic coordinates. However, since we are interested in the orbit description in geomagnetic latitude and magnetic local time there will be a seasonal rotation of the orbits because of the seasonal dependence of magnetic local time. (See Whalen, 1970). Figure 3 shows the rotation for Winter, Spring, Summer and Fall seasons. The maximum rotation is approximately 40 minutes. The polar cap coverage remains essentially the same throughout the satellite lifetime.

The dawn-dusk series of DMSP satellites appear to be particularly useful satellites to determine auroral boundaries since two equatorward boundaries are crossed in a given pole every 100 minutes. However, equatorward boundaries, even for a given magnetic activity are known to be asymmetric in local time. (See Appendix I to this Report). In fact, Meng (1977) and Rossberg (1978) find that for quiet times the best representation of the auroral oval is a circle whose center is offset from the magnetic pole toward the midnight sector by about  $4^\circ$ . This asymmetry will lead to a universal time variation in boundary measurements even though there is, in fact, no change in the oval. To show this we superimposed in Figure 4 an offset circle, offset by  $4^\circ$  toward midnight, of radius  $20^\circ$  on a north polar cap with the DMSP-F2 orbits of Figure 1. The intersections of the paths with the offset circle will constitute the equatorward edge of the oval. These positions are plotted in Figures 5 and 6 for dawn and dusk boundaries. The circles connected with a line are for the north pole; the triangles are for similar positions in the south pole. There is, of course, a variation in equatorward edge of nearly  $4^\circ$  since most of the offset will be realized in the dawn and dusk regions.

Thus, it cannot be too firmly stressed, that any attempt to use DMSP Satellite auroral boundaries (or those from any other satellite, for that matter) to determine the state of the high latitude regions, must, for any

kind of consistency, take into account the local time variation of the oval boundaries for given magnetic activities.

## 2. Description of the Experiment and Calibration Results.

The first four SSJ/3 detectors to be flown on the F2, F3, F4 and F5 satellites are identical in design. They are built to measure the flux of electrons incident to the spacecraft in 16 energy bins spanning in energy from 50eV to 20,000eV. This is accomplished using two sets of curved plates that are sequenced through 8 voltage levels in tandem each second. The detector dwells for a period of 98 milliseconds in each channel with 2 milliseconds being left between steps to stabilize the voltage. The plates sequence from high voltage to low and after the 8th level the detector holds for 200 milliseconds before restarting the sequence.

The DMSP satellites are non-spinning. The SSJ/3 sensors are mounted on the satellite such that their look direction is oriented radially outward from the earth at all times. The total package weighs 3.046 lbs and consumes .125 watts of power.

The first two detectors were calibrated using Monte Carlo techniques and limited analysis with a beam system. This work has been reported on previously (Huber et al., 1977). The third and forth detectors(on F4 and F5) were calibrated using an electron beam system at Rice University in Houston, Texas. We report here the calibration results of the third and fourth detectors even though the geometric factors obtained by Huber are used in the data reduction for F2 currently in orbit. We feel that comparison of the earlier calibration results with the more extensive method used here will at least verify to a specified accuracy the earlier calibrations, if not make possible corrections to the geometric factors now used.



7

The electron beam system consists of an aluminum plate irradiated by a set of UV lamps. The photoelectrons driven off the plate by the UV are accelerated by a series of grids between the plate and the detector to be calibrated. The instrument to be calibrated is mounted on a fixture such that the look direction of the detector can be positioned at any angle desired relative to the beam. The system produced a homogeneous beam of electrons with an ~18 inch radius. The energy of the beam is turnable in energy from approximately 30 volts to 35000 volts. The entire system is contained within a set of Hemholz coils used to cancel out the earth's magnetic field.

The calibration system is computer controlled such that it automatically sequences through a two dimensional array of angles relative to the detector aperture for any fixed energy of the incident beam. The counts accumulated as the detector dwells at each angular position are stored in core and recorded onto magnetic tape. The current density in the beam is determined using a Faraday cup that is shifted into the beam at the beginning of each angular scan. The counts observed over a typical angular scan are shown in Figure 7.

At the end of each scan the computer calculates the energy dependent geometric factor,  $G(E)$ . By determining  $G(E)$  at a series of energies one can approximate the response curve for each fixed voltage on the plates. The response curve allows one to determine the channel pass band,  $\Delta E$ , and by integrating over the response curve one can calculate the energy independent geometric factor  $G$ .  $G$  is defined such that

$$j(E) = \frac{C / \Delta T}{G} \quad (1)$$

where  $j(E)$  is the differential flux (electrons/cm<sup>2</sup>-sec ster.-eV) in the channel with central energy  $E$ ,  $C$  is the count observed in that channel,  $\Delta T$ , is the accumulation interval for these counts.  $G$  is given in units of cm<sup>2</sup>-ster.-eV.

In the Rice calibration the SSJ/3 detectors for the F-4 and F-5 satellites were

mounted in the chamber together, with the Faraday cup in between the two detectors. Approximately two hundred angular scans were made to map the response curves for the sixteen channels. In Figure 8a and 8b we show the representative response curves. Each plot contains the response curves from both detectors.

There are several points of note in reference to these curves. In the following we will refer to detectors 4 and 5 depending on whether we are considering the detector for the F-4 or F-5 satellites respectively. One notes that for channel 8 the results from the two detectors are in excellent agreement. The central energies agree to within 1% and the peak values of  $G(E)$  to within 6%. The shapes of the response curves are almost identical. For channel 9 the agreement is not quite as good. In this case the peak values of  $G(E)$  differ by approximately 15% ( $4.5 \times 10^{-4}$  for detector 4 as opposed to  $3.8 \times 10^{-4}$  for detector 5) and the width of the response curves also differ ( $\Delta E/E$  of .10 as opposed to .131 for detector 4 and 5 respectively). The reason for the difference is at present not understood.

The angular resolution of the detectors was determined by looking at the response of channels 8 and 9 at approximately their central energies in directions perpendicular and parallel to the two cylindrical plates of the analyzer. The two angles  $\alpha$  and  $\beta$  are shown in Figure 9 and the response curves for variations in both angles are shown in Figure 10 through 11. In the figures the response has been normalized to the counts observed where  $\alpha = \beta = 0$ .  $\Delta\alpha$  and  $\Delta\beta$  are defined as the full width at half maximim of the angular response. The values for  $\Delta\alpha$  and  $\Delta\beta$  for the two detectors are



$\Delta\alpha$ (Channel 8)		$\Delta\alpha$ (Channel 9)	
Detector 4	Detector 5	Detector 4	Detector 5
2.0°	1.8°	3.85°	3.50°
$\Delta\beta$ (Channel 8)		$\Delta\beta$ (Channel 9)	
Detector 4	Detector 5	Detector 4	Detector 5
10.45°	8.8°	4.60°	4.60°

The two detectors are in close agreement except for  $\Delta\beta$  in Channel 8 where the two detectors differ by approximately 15%.

For channels 1 through 8 the calibration gave excellent results. We have listed in Table 1 the peak energy, the full width at half maximum, the peak value of  $G(E)$  and the integrated energy independent geometric factor for each channel. The peak value of  $G(E)$  decreases with increasing energies from a value of approximately  $1.1 \times 10^{-3}$  at 1 KeV to  $\sim 8 \times 10^{-4}$  at 20 KeV. This arises from a decrease in channeltron efficiency with increasing energy.

It is important to compare the observed decrease in channeltron efficiency to that predicted from the work of Archuleta and DeForest (1971). They maintain that the efficiency of a channel electron multiplier between 1 KeV and 50 MeV has a functional form

$$\epsilon = 1.0 - \left[ 3.0 + \frac{2.0}{\frac{6.5}{(E + .05)} + \frac{30}{(E + .05)^3}} \right] \quad (2)$$

where  $E$  is expressed in KeV. We have found the shape of the response curve to remain the same for all the channels above 1 KeV. The decrease in the peak value we attribute, therefore, exclusively to a change in channeltron efficiency.

Table 1

Channel	E Peak		$\Delta E$		G Peak		$G(E)dE$	
	#4	#5	#4	#5	#4	#5	#4	#5
1	20200eV	20640eV	1880eV	1860eV	4.0x10 <sup>-4</sup>	4.1x10 <sup>-4</sup>	7.98x10 <sup>-1</sup>	8.53x10 <sup>-1</sup>
2	13160eV	13200eV	1280eV	1310eV	4.8x10 <sup>-4</sup>	5.2x10 <sup>-4</sup>	6.35x10 <sup>-1</sup>	6.99x10 <sup>-1</sup>
3	8480eV	8550eV	760eV	785eV	6.1x10 <sup>-4</sup>	6.4x10 <sup>-4</sup>	4.83x10 <sup>-1</sup>	5.22x10 <sup>-1</sup>
4	5500eV	5550eV	483eV	509eV	7.2x10 <sup>-4</sup>	7.4x10 <sup>-4</sup>	3.61x10 <sup>-1</sup>	3.88x10 <sup>-1</sup>
5	3575eV	3590eV	322eV	327eV	8.21x10 <sup>-4</sup>	8.5x10 <sup>-4</sup>	2.71x10 <sup>-1</sup>	2.94x10 <sup>-1</sup>
6	2350eV	2365eV	205eV	216eV	9.1x10 <sup>-4</sup>	9.4x10 <sup>-4</sup>	1.98x10 <sup>-1</sup>	2.07x10 <sup>-1</sup>
7	1525eV	1550eV	138eV	151eV	1.0x10 <sup>-3</sup>	1.0x10 <sup>-3</sup>	1.46x10 <sup>-1</sup>	1.54x10 <sup>-1</sup>
8	997eV	1003eV	100eV	99eV	1.06x10 <sup>-3</sup>	1.13x10 <sup>-3</sup>	1.08x10 <sup>-1</sup>	1.10x10 <sup>-1</sup>
9	972eV	975eV	127eV	103eV	3.80x10 <sup>-4</sup>	4.50x10 <sup>-4</sup>	4.83x10 <sup>-2</sup>	4.64x10 <sup>-2</sup>
10	638eV	638eV	84eV	68eV	3.90x10 <sup>-4</sup>	4.50x10 <sup>-4</sup>	3.28x10 <sup>-2</sup>	3.06x10 <sup>-2</sup>
11	414eV	410eV	54eV	43eV	3.80x10 <sup>-4</sup>	4.50x10 <sup>-4</sup>	2.05x10 <sup>-2</sup>	1.94x10 <sup>-2</sup>
12	267eV	267eV	35eV	28eV	3.80x10 <sup>-4</sup>	4.50x10 <sup>-4</sup>	1.33x10 <sup>-2</sup>	1.26x10 <sup>-2</sup>
13	173eV	173eV	23eV	18eV	3.80x10 <sup>-4</sup>	4.50x10 <sup>-4</sup>	8.74x10 <sup>-3</sup>	8.10x10 <sup>-3</sup>
14	112eV	113eV	15eV	12eV	3.80x10 <sup>-4</sup>	4.70x10 <sup>-4</sup>	5.70x10 <sup>-3</sup>	5.60x10 <sup>-3</sup>
15	73.0eV	72.2eV	9.6eV	9.6eV	3.80x10 <sup>-4</sup>	4.50x10 <sup>-4</sup>	3.65x10 <sup>-3</sup>	3.42x10 <sup>-3</sup>
16	47.0eV	46.6eV	6.1eV	4.9eV	2.89x10 <sup>-4</sup>	3.40x10 <sup>-4</sup>	1.76x10 <sup>-3</sup>	1.67x10 <sup>-3</sup>



We assume the efficiency in channel 8 is unity and have taken the ratio of the peak value of  $G(E)$  in preceding channels to the peak value of  $G(E)$  in channel 8 to give the efficiency. In Table 2 we have listed the efficiencies determined in this manner together with the values predicted from equation 2. One notes that in the energy range from 2 KeV to 10 KeV the efficiencies derived in this manner are between 10% and 20% higher than those predicted while they are in substantial agreement outside this range.

For the four channels 9-16 the calibration also yielded consistent results. The peak value for  $G(E)$  in these channels is  $3.8 \times 10^{-4}$  and  $4.5 \times 10^{-4}$  respectively for detector 4 and 5 and the value of  $\Delta E/E$  is constant as cited previously. The one exception is channel 11 for detector 4. For this case the line shape was maintained but the peak value of  $G(E)$  was  $5.28 \times 10^{-4}$ .

We attribute the anomalously high value to small inhomogeneities in the calibrating beam. As we pointed out before the beam is produced by illuminating an aluminum plate with a set of UV lamps. The illumination is not perfectly uniform leading to small inhomogeneities in the beam intensity. As the beam energy is decreased the radius of curvature for electrons, in whatever residual field that remains within the Helmholtz coils, decreases shifting the orientation of the beam slightly. For the calibration of a specific channel such a shift can place one of these small inhomogeneities at the entrance aperture of one of the detectors. If the beam is more intense in the small region this can lead to an erroneously high value of  $G(E)$  as was observed. We believe this to be the explanation for the results for channel 11 and have assigned it, therefore, the same peak  $G(E)$  as the surrounding channels.

Table 2

## EFFICIENCY

Energy	Detector 4	Detector 5	Archeletor & Deforest	% Difference Detector 4	% Difference Detector 5
20000eV	.36	.39	.405	-11%	-4%
13000eV	.46	.45	.43	7%	5%
8500eV	.57	.58	.48	19%	21%
5500eV	.65	.68	.56	16%	22%
3575eV	.75	.77	.66	14%	17%
2350eV	.83	.86	.83	0%	4%
1550eV	.88	.94	.94	6%	0%
1000eV	1.00	1.00	.99	0%	0%

For channels 13 through 16 difficulties were encountered in adjusting the Helmholtz coils to correct for the earth's magnetic field and in maintaining a uniform mono directional beam. Reasonable numbers were determined for central energy of each channel but the peak value of  $G(E)$  and  $\Delta E/E$  were assumed to be the same as for the four higher energy channels. For channels 13 through 15 the channeltron efficiency should be unity. For channel 16 the efficiency was calculated from the equation

$$E_e = .10E^{0.515}(E \text{ in eV}) \quad (3)$$

from the work of Archuleta and DeForest (1971). All the calibration numbers are listed in Table 1.

In Figures 12-17 we show the normalized curves for channels 1-8 and 9-12 for detectors 4 and 5. The curves were calculated by normalizing the measurements of  $G(E)$  observed in a given channel to the peak value  $G_0(E)$  observed in that channel and by normalizing the energy,  $E$ , at which each measurement was made to the central energy of the channel  $E_0$ . The geometric factors obtained for F2 and F3 by Huber et al., (1977) using Monte Carlo techniques are compared to those for F3 and F4 in Table 3. In general the overall agreement is between 10% and 20%. For channels 1-8 the values for the beam calibration are 10 to 20% lower than those from the previous calibration. For channels 9 through 16 the beam calibration gives numbers 10 to 20% higher than from the work of Huber et al., (1977). We attribute the difference to instrumental uncertainties between the two calibration systems. We believe, however, that the beam calibration at Rice University provides basically more accurate numbers and should be used in future processing.



TABLE 3  
SG(E)dE

CHANNEL	#4	#5	#2 & #3
1	$7.98 \times 10^{-1}$	$8.53 \times 10^{-1}$	1.05
2	$6.35 \times 10^{-1}$	$6.99 \times 10^{-1}$	$7.66 \times 10^{-1}$
3	$4.83 \times 10^{-1}$	$5.22 \times 10^{-1}$	$5.59 \times 10^{-1}$
4	$3.61 \times 10^{-1}$	$3.88 \times 10^{-1}$	$4.00 \times 10^{-1}$
5	$2.71 \times 10^{-1}$	$2.94 \times 10^{-1}$	$3.25 \times 10^{-1}$
6	$1.98 \times 10^{-1}$	$2.47 \times 10^{-1}$	$2.47 \times 10^{-1}$
7	$1.46 \times 10^{-1}$	$1.54 \times 10^{-1}$	$1.94 \times 10^{-1}$
8	$1.08 \times 10^{-1}$	$1.10 \times 10^{-1}$	$1.36 \times 10^{-1}$
9	$4.83 \times 10^{-2}$	$4.64 \times 10^{-2}$	$4.49 \times 10^{-2}$
10	$3.28 \times 10^{-2}$	$3.06 \times 10^{-2}$	$2.84 \times 10^{-2}$
11	$2.05 \times 10^{-2}$	$1.94 \times 10^{-2}$	$1.86 \times 10^{-2}$
12	$1.33 \times 10^{-2}$	$1.26 \times 10^{-2}$	$1.13 \times 10^{-2}$
13	$8.74 \times 10^{-3}$	$8.10 \times 10^{-3}$	$7.86 \times 10^{-3}$
14	$5.70 \times 10^{-3}$	$5.60 \times 10^{-3}$	$3.31 \times 10^{-3}$
15	$3.65 \times 10^{-3}$	$3.42 \times 10^{-3}$	$3.31 \times 10^{-3}$
16	$1.76 \times 10^{-3}$	$1.67 \times 10^{-3}$	$1.67 \times 10^{-3}$



### 3. Data Reduction of SSJ/3 on DMSP-F2 as performed at AFGL.

The precipitating electron data from DMSP-F2 are displayed as shown in Figure 18. The data is taken from a south pole pass on July 2, 1978. For each satellite pass the following are plotted as a function of universal time:

- a) The total number flux or integral flux, JTOT.

$$JTOT = \sum_i j(E_i) \frac{E_{i+1} - E_{i-1}}{2}, \quad (4)$$

where  $j(E_i)$  is the differential flux for each energy channel with central energy  $E_i$ . The differential flux is calculated from the count rate by the equation.

$$j(E_i) = \frac{C_i / \Delta T}{G(E_i) \Delta E_i} \quad (5)$$

with  $C_i$ , the counts in the accumulation interval  $\Delta T$ ,  $G(E_i)$ , the energy dependent geometric factor and  $\Delta E_i$ , the channel width. The total number flux is measured in particles/(cm<sup>2</sup>.ster.sec.);

- b) The integral energy flux JETOT

$$JETOT = \sum_i E_i j(E_i) \left( \frac{E_{i+1} - E_{i-1}}{2} \right) \quad (6)$$

and is measured in KeV/(cm<sup>2</sup>.ster.sec.);

- c) The average energy, EAV.

$$EAV = \frac{JETOT}{JTOT} \quad (7)$$

The energy is in KeV, and the scale for the average energy is linear.

The universal time is given in seconds with an interval of one minute between tick marks. At two minute intervals ephemeris data is given. The values given are the geographic coordinates of the satellite, the corrected geomagnetic coordinates of the satellite projected along the magnetic field line to 100 km, and the magnetic local time.

The satellite pass in Figure 18 is not to be taken as representative.

It is, if anything, too clean; but as such is useful for discussion of various features of the data. The vertical lines are the best estimates, from changes in the number flux and the energy flux, of the auroral boundaries, both equatorward and poleward. Equatorward of both equatorward boundaries (morning and evening) are regions in which the energy flux and the average energy are inflated. A lesser inflation of the number flux occurs. These increases are produced by high energy particles from the inner radiation belts that penetrate through the detector casing stimulating the spiraltron directly and giving spurious counts. For moderate and low magnetic activities there is usually a well-defined gap between oval data and inner radiation belt data making it easy to identify and disregard the latter. At higher activities the oval moves equatorward and the two regions can overlap. In these cases care must be taken to differentiate the two populations.

For the case shown in Figure 18 the boundaries have the sharpest changes in the energy flux. However, many times a more gradual transition from background in both number and energy fluxes is the case. An example, although not a troublesome one, occurs on the equatorward morning edge in the number flux. Fortunately, the energy flux transition is considerably sharper.

We have found that for cases such that shown in Figure 18, the oval boundaries we choose from sharp changes in the fluxes correspond closely to the positions where the number flux rises and remains for at least a short period of time above the  $10^7$  level. In the case shown the boundaries determined by both methods are identical (as shown by the horizontal line at the  $10^7$  level). In Section 4 we will look at the feasibility of using the  $10^7$  level in the number flux as a way of standardizing the definition



of auroral boundaries.

As pointed out in Section 1 dawn-to-dusk coverage of the auroral regions, and the caps, is obtainable only for DMSP-F2 in the first 11 hours of UT. After this time the north pole subsatellite track lies below  $80^\circ$  often remaining in the midnight sector throughout. Figure 19 shows a north pole pass later on July 2, 1978. The equatorward boundaries are clear and are marked. Poleward, however, there is continuity in all quantities from morning to evening making it unclear where the satellite enters the polar cap, if at all. Figure 20 shows a south pole pass at approximately 13:30 UT. The subsatellite track passes through the midday region near the cusp, and again, never clearly enters the polar cap. The equatorward boundaries, as determined by the criterion  $JTOT > 10^7$ , are designated. There is some structure equatorward of these boundaries, particularly on the evening side that is not associated with spurious counts from inner radiation belt particles. The south pole pass, one pass later, is shown in Figure 21. Here the the subsatellite track passing below the cusp misses the oval entirely.

In Figures 22-24 we demonstrate the total information capacity of DMSP-F2 in dealing with the auroral regions. Figure 22 shows the DMSP image from January 3, 1978 at around 15 UT gridded in corrected geomagnetic coordinates. Figure 23 is the corresponding precipitating electron data in the form we have discussed. Figure 24 shows ten differential energy spectra for ten successive seconds showing the transition from the most equatorward discrete arc in the evening to the evening diffuse aurora. A display of spectra such as this is available for any ten second interval throughout the high latitude pass.



#### 4. Examination of Data from Four Passes.

In the following the precipitating electron data for four passes (successive north-south pole passes during an active time and successive north-south pole passes during a quiet time) in the format discussed above are examined. We are particularly interested in determining oval (and, therefore, cap) boundaries in a consistent way from the data. From an examination of two months of data it appeared that choosing the position where the total number flux first rose and then fell from  $10^7$  particles/ster.cm<sup>2</sup>.sec. was a good definition of the equatorward and polar boundaries. Therefore, the primary focus of the discussion of the four passes will be boundary determination and the problems involved in this process. Other points of interest will be mentioned as well.

The precipitating electron data are given in Figures 25-28.

##### A. North Pole Active: February 28, 1978; Kp = 5+ (Figure 25).

###### i. Evening Equatorward

The equatorward boundary is placed at 63.0° (magnetic latitude).

The JTOT =  $10^7$  boundary is identical to the best choice of where JTOT rises out of background. The rise is fairly steep.

For JETOT and EAV the expanded oval values begin to overlap the spurious counts from the inner radiation belt, obscuring the equatorward boundary.

EAV rises from background levels approximately 1° higher than the equatorward boundary, or at 64°. This is also the approximate place where JETOT >  $10^8$ : a minimum value for auroral forms to be seen in DMSP images. The rise in average energy above 64° is very steep.

###### ii. Evening Poleward

The poleward boundary is placed at  $73.9^\circ$ .

Again the  $JTOT = 10^7$  boundary and the best choice of all parameters falling back to background levels are identical. In this case, the last visible arc on DMSP (where  $JE\ TOT > 10^8$ ) and the poleward boundary are nearly coincident.

### iii. Morning Equatorward

The morning equatorward boundary using the  $JTOT = 10^7$  criterion is  $55.8^\circ$ . This is, as well, the position for the  $JTOT$  and  $JETOT$  rise from background. However, the rise is very slow; and even though the rise is associated with a rise in average energy this boundary is nearly  $10^\circ$  lower than the boundary at which  $JETOT$  is above the threshold for visible auroras. ( $JETOT > 10^8$  occurs at  $65^\circ$ ). That the slow rise might be due to spurious counts due to penetrating particles is rejected since the modulation in the average energy is not characteristic of that for spurious counts. Since the selection of the boundary is so dependent on the criterion used some ambiguity remains for cases such as these.

### iv. Morning Poleward

The morning poleward boundary cannot be assuredly determined because of the data gap (caused by the transmission of data to ground). It appears, however, that the gap lies just poleward of the position where  $JETOT$  and  $JTOT$  fall to background.

Characteristic of morning poleward electron fluxes is high variability in  $JTOT$  and  $JETOT$ , while the equatorward values are more uniformly increasing, suggestive of two distinct types of electron population that are contiguous. If two such populations also exist on the evening side they would have to be superposed to a much greater



extent than in the morning to give the observing variations in the fluxes there. The variable morning population has, in this case, considerably lower average energy than the more uniform equatorward population.

Typically the peak average energy in the morning is greater than that in the evening although for this case the difference is not great.

B. South Pole Active: February 28, 1978;  $K_p = 4+$  (Figure 26).

This is the pass following the north pole pass discussed above.

#### 1. Evening Equatorward.

The equatorward boundary is placed at  $-61.9^\circ$  using the criterion that  $JTOT > 10^7$ . This choice gives a value somewhat higher than the position of JTOT rising out of background. However, it appears from the average energy values equatorward of this boundary that the small rise in number flux may be caused by the spurious counts. In any case the  $10^7$  method places the boundary at the sharpest change in number and energy fluxes and is near the position at which  $JETOT \sim 10^8$  (on the position of near-visible aurora). As in the north pole active case, the strong rise in average energy occurs considerably poleward of this boundary.

#### ii. Evening Poleward

The evening poleward boundary is placed at  $-74.9^\circ$ . Sharp discontinuities in all quantities as well as the  $JTOT = 10^7$  position occur at this value.

There are variations in the number flux across the cap which rise briefly to values as much as  $10^7$ , which were they stronger could cause ambiguity in determining a poleward boundary.



### iii. Morning Equatorward

As in the north pole active case the morning equatorward boundary presents two choices, quite different and made more problematic by the spurious counts which occur in the region where the number flux is rising out of background. The  $JTOT = 10^7$  boundary is at  $-58.5^\circ$  and is suspect because of the spurious data. Discontinuities in the energy flux and the average energy occur at  $-64.7$  and probably provide the more reliable estimate.

### iv. Morning Poleward

The morning poleward boundary is placed at  $-72.6$ . The south pole boundary is clearer than the corresponding north pole boundary, the background fluxes being less continuous into the cap than seen in Figure 25. Fluxes greater than  $10^7$  do arise, however, out of the background at higher latitudes. If we required all fluctuations in the number flux to remain below the  $10^7$  level, the morning poleward boundary would be placed at  $-79.6^\circ$ .

Some comments on the active cases.

The polar caps are quite evident in the two active cases discussed here. The polar cap fluxes in the north pole show a smooth variation from  $\sim 4 \cdot 10^6 \frac{\text{particles}}{\text{ster cm}^2 \text{ sec}}$  in the morning to  $\sim 4 \cdot 10^5 \frac{\text{particles}}{\text{ster cm}^2 \text{ sec}}$  in the evening. In the south pole the fluxes vary in the opposite sense, a phenomenon discussed by Meng (1977) and related by him to the y-component of the interplanetary magnetic field. According to Meng the flux gradient shown here would indicate a positive y-component in the IMF. The provisional indices for February, 1978 show an away sector at this time (Lincoln, 1978b) which normally occur with positive  $B_y$ . The south pole fluxes are more variable than those in the

north pole but range from  $10^6$  -  $10^7$  particles/ster  $\text{cm}^2$  sec, more than double the north pole range.

The equatorward background levels in the south pole are lower than in the north pole as would be expected if the electron population producing this background level is primarily photoelectrons in this region. The south pole is in daylight and produces more photoelectrons than the north pole. These low energy electrons travel up the field line and precipitate in the conjugate hemisphere and are detected by the J-sensors.

The evening boundaries are much sharper than the morning boundaries, there being strong discontinuities in the fluxes there. The general trend of the total fluxes in the morning oval is much more continuous for both boundaries and more slowly varying.

C. North Pole Quiet: January 21, 1978,  $K_p = 0$ . (Figure 27).

The boundaries determined by the  $10^7$  limit in particle flux background levels (ignoring polar scatter and the equatorward spur on the evening side) are:

	<u>Equatorward</u>	<u>Poleward</u>
Morning	70.5°	84.3°
Evening	72.1°	82.7°

It is apparent, however, that the assignment of poleward boundaries has very little meaning: the variations in both the number and the energy flux are completely continuous, i.e. bowl-shaped across the cap. The morning poleward signature discussed for the active cases, i.e. considerable variability in fluxes poleward of smooth fluxes, is present here, both on the morning and evening sides of the oval.

There is a small spur of high energy particles equatorward of the  $10^7$  boundary on the evening side. It is clear that whatever leads to a sharp differentiation between the cap and oval in active times is absent for the quiet time shown here. If asymmetric convection is the cause of particle gradients in the cap as suggested by Meng (1977) they may be considerably lessened or less asymmetric in quiet times. (Provisional data of Lincoln, 1978a, shows the IMF to be in an away sector here as well).

The average energies are considerably reduced for quiet times. The peak average energy in the morning is greater than that in the evening.

The minimum number flux in the cap is  $\sim 4 \cdot 10^6 \frac{\text{particles}}{\text{ster cm}^2 \text{ sec}}$ .

D. South Pole Quiet: January 21, 1978,  $K_p = 0$ . (Figure 28)

The south polar cap is more clearly defined than the north polar cap, being a region of comparatively low, uniform flux. The flux in the cap, however, is higher than that in the north pole, reaching values of  $10^7$  particles/ster  $\text{cm}^2 \text{ sec}$ . If slightly higher, such fluxes would preclude use of the  $10^7$ /level. Nevertheless, we continue to use it here. The  $10^7$  boundaries are

	<u>Equatorward</u>	<u>Poleward</u>
Morning	-70.9°	-86.6°
Evening	-71.2°	-85.4°

There is an interesting spur-like feature below the evening equatorward boundary which remains for several passes, exceeding the  $10^7$  level in JTOT. In this case the spur is not a problem and, in general, such problems can be avoided if we require flux levels to reach and stay at or above  $10^7$ . The evening oval for this very quiet time has almost no modulation in the average energy.



For both quiet time cases the total energy flux is below the needed threshold to produce arcs detectable by DMSP. Despite this fact, the electron precipitation reveals a fairly well-defined oval and cap structure: at least as well-defined as for active times, although the problems of definition are somewhat different.

In Figure 29 we compare the oval boundaries for the four cases. The heavy lines are the boundaries determined by the  $10^7$  criterion. The dashed lines indicate other determinations of the boundaries as discussed in the text. The shaded area denotes the variation in boundary definition. Two points stand out:

- a) the boundaries are highly variable.
- b) There are fewer discrepancies (none here) in determining both the evening boundaries. Both poleward and equatorward boundaries in the morning side are difficult to determine in a consistent way independent of magnetic activity.

In addition to the problems in determining auroral boundaries we find the cases discussed here representative of much of the data we have surveyed in the following ways:

- a) The morning oval is wider than the evening oval.
- b) The fluxes, number and energy, in the morning oval seem to be composed of two contiguous parts: a smoothly varying equatorward region with small fluctuations; a highly varying poleward part. The morning oval always has this composition. At times the evening oval can have a similar composition, but it more typically appears to be similar to the equatorward region in the morning with somewhat greater fluctuations and sharper boundaries. An alternative description is a single region that would result if the two morning regions were superimposed.

c) The polar cap fluxes are here remarkably smooth and low between  $2.10^5$  and  $2.10^6$  particles/ster  $\text{cm}^2\text{sec}$ . The low number count rates are reflected in the large statistical scatter in the average energy.

d) The average energy has more gradual transitions inside the oval than the fluxes.

e) The peak average energy is generally higher in the morning than the evening.

f) The equatorward oval boundaries are reasonably symmetrical dawn to dusk.

The poleward oval boundaries are highly asymmetric as a result of the larger morning oval. The morning poleward boundary often reaches values  $>80^\circ$  magnetic latitude.

From this lengthy analysis of four passes several questions suggest themselves regarding the use of this data to monitor real time magnetospheric and solar wind conditions.

1. If we wish to have a real time indicator of auroral activity by making use of equatorward boundaries in electron particle precipitation should we confine that determination to the more well-behaved evening sector?

2. Is there a better indicator of auroral activity than oval boundaries; perhaps, the peak in the average energy?

3. Can the difference in polar fluxes be used to determine IMF sectors. If so, can it be made quantitative as well?

4. Is there a near constant particle flux into the polar regions irrespective of magnetic activity? The evening oval size as shown in Figure 29 remains remarkably the same for the wide span in activity,

and the number fluxes for active and quiet times are quite comparable.  
(Compare Figures 25-28) Does this indicate a steady source of electrons  
with major variations between quiet and active times caused by variations  
in acceleration mechanisms?



## REFERENCES

- Archuleta, R.J., and S.E. DeForest, Efficiency of channel electron multipliers for electrons of 1-50 keV, Rev. of Sci. Instru., 42, 89, 1971.
- Candidi, M., H.W. Kroehl, G. Kosinski and R.W. Buhmann, DMSP-F2 observations of cusplike electron precipitation regions during the September 19-21, 1977 event, Space. Sci. Rev. 22, 667, 1978.
- Eather, R.H., DMSP Calibration (to be published), 1979.
- Foster, J.C., and J.R. Burrows, Electron fluxes over the polar cap, 1, Intense keV fluxes during poststorm quieting, J. Geophys. Res., 81, 6016, 1976.
- Huber, A., J. Pantazis, A.L. Besse, and P.L. Rothwell: 1977, Calibration of the SSJ/3 Sensor on the DMSP Satellites, AFGL-TR-77-0202 Scientific Report No. 2, September 1977.
- Lincoln, J. Virginia, Geomagnetic and solar data, J. Geophys. Res., 83, 232, 1978 a.
- Lincoln, J. Virginia, Geomagnetic and solar data, J. Geophys. Res., 83, 744, 1978b.
- Mende, S.B., and R.H. Eather, Monochromatic all-sky observations and auroral precipitation patterns., J. Geophys. Res., 81, 3771, 1976.
- Meng, C.-I., R.H. Holzworth, and S.-I. Akasofu, Auroral circle-delineating the poleward boundary of the quiet auroral belt, J. Geophys. Res., 82, 164, 1977.
- Meng, C.-I., and H.W. Kroehl, Intense uniform precipitation of low-energy electrons over the polar cap, J. Geophys. Res., 82, 2305, 1977.
- Mizera., P.F., D.R. Croley Jr., F.A. Morse and A.L. Vampola, Electron fluxes and correlations with quiet time auroral arcs, J. Geophys. Res., 80, 2129, 1975.
- Mizera, P.F. and J.F. Fennell, Satellite observations of polar, magnetotail lobe, and interplanetary electrons at low energies, Rev. Geophys. Space Phys., 16, 147, 1978.
- Rossberg, L., Undisturbed trapping boundary for energetic electrons at low altitudes, J. Geophys. Res., 83, 4307, 1978.
- Smiddy, M., R.C. Sagalyn, W.P. Sullivan, P.J.L. Wildman, P. Anderson and F. Rich, The Topside Ionosphere Plasma Monitor (SSIE) for the Block 5D/Flight 2 DMSP Satellite, AFGL-TR-78-0071 Instrumentation Papers, No. 266, March 1978.
- Whalen, James A., Auroral Oval Plotter and Nomograph for Determining Corrected Geomagnetic Local Time, Latitude and Longitude for High Latitudes in the Northern Hemisphere, AFCRL-70-0422

## FIGURE CAPTIONS

- Figure 1: The DMSP-F2 satellite paths over the North polar regions for given universal times; plotted in corrected geomagnetic latitude and magnetic local time. (Data taken from February, 1978 passes).
- Figure 2: Same as Figure 1, but for South polar regions.
- Figure 3: The seasonal dependence of the DMSP-F2 satellite path between 06-07 UT over the North polar region; plotted in corrected geomagnetic latitude and magnetic local time. The days for which the data are taken are shown in the legend.
- Figure 4: A representation (the double-dashed line) of the quiet time auroral oval: a circle offset from the geomagnetic pole  $4^\circ$  toward midnight and of radius  $20^\circ$ ; superposed on the North polar satellite paths of DMSP-F2 plotted in corrected geomagnetic latitude and magnetic local time, as shown in Figure 1.
- Figure 5: The universal time variation in the morning equatorward auroral boundary that would be measured by DMSP-F2 if the equatorward oval boundary were a circle offset from the geomagnetic pole  $4^\circ$  toward midnight and of radius  $20^\circ$ . The connected dots show variations for the North pole equatorward boundary; the triangles for the South pole.
- Figure 6: Same as Figure 5, but for evening equatorward boundaries.
- Figure 7: The angular response of detector 4 in channel 8 to a beam with an energy of 985 eV. The angles  $\alpha$  and  $\beta$  are measured in two orthogonal directions relative to the normal to the detector aperture.
- Figure 8a: The energy dependent geometric factor,  $G(E)$ , plotted as a function of energy for channel 8 of detectors 4 and 5.
- Figure 8b: The energy dependent geometric factor,  $G(E)$ , plotted as a function of energy for channel 9 of detectors 4 and 5.
- Figure 9: Details of the configuration of the apertures and curved plated of the analyzer showing the angles  $\alpha$  and  $\beta$ .
- Figure 10: Angular response of detectors 4 and 5 on channel 8. For  $\beta$  the curve is the response along the axis where  $\alpha = 0$  and is normalized to the counts observed when  $\alpha = \beta = 0$ . Similarly for  $\alpha$  the curve is the response along the axis where  $\beta = 0$  and is normalized to the counts observed when  $\alpha = \beta = 0$ .



- Figure 11: The same as Figure 10 but for channel 9 of detectors 4 and 5.
- Figure 12: The energy dependent geometric factor,  $G(E)$  normalized to the peak geometric factor  $G_0(E_0)$  plotted as a function of energy normalized to the channels central energy,  $E_0$ . The figure shows the data from channels 9 through 12 for detector 5.
- Figure 13: Same as Figure 12 but for detector 4.
- Figure 14: Normalized curves of the energy dependent geometric factor as in Figure 12 for channels 1 through 4 of detector 4.
- Figure 15: Same as Figure 14 but for channels 5 through 8 of detector 4.
- Figure 16: Same as Figure 14 but for channels 1 through 4 of detector 5.
- Figure 17: Same as Figure 14 but for channels 5 through 8 of detector 5.
- Figure 18: The format in which the DMSP-F2 precipitating electron data is processed. The first panel gives the average energy in keV (the scale is linear); the second panel gives the integral energy flux, JETOT, in  $\text{keV}/\text{cm}^2\text{ster. sec.}$ ; the third panel gives the total number flux, JTOT in  $\text{electrons}/(\text{cm}^2\text{ster. sec.})$ . These values are plotted against the following: universal time, geographic coordinates of the satellite, corrected geomagnetic coordinates of the satellite projected along the magnetic field line to 100 km, and the magnetic local time. The data is taken on July 2, 1978. The vertical lines indicate equatorward and poleward oval boundaries, as determined from changes in the number and energy fluxes.
- Figure 19: Same as Figure 18, but for a later UT in which the satellite path does not enter the North polar cap, but passes through the midnight oval.
- Figure 20: Same as Figure 18, but for a later UT in which the satellite path does not enter the South polar cap, but passes through the midday oval, or the cusp region.
- Figure 21: Same as Figure 20, but for a later UT in which the satellite path is always equatorward of the midday oval.



- Figure 22: The DMSP-F2 image for January 3, 1978, near 15 UT gridded in corrected geomagnetic coordinates.
- Figure 23: The precipitating electron data for the DMSP-F2 pass on January 3, 1978, near 15 UT, whose auroral image is shown in Figure 22. The format is the same as that for Figure 18.
- Figure 24: Ten differential energy spectra for ten successive seconds of DMSP-F2 precipitating electron data taken on January 3, 1978 at 15-18-5 to 15-18-14 UT.
- Figure 25: DMSP-F2 precipitating electron data for a North polar pass during high magnetic activity. Equatorward and poleward oval boundaries are marked by vertical lines. See text for a discussion of the methods used for boundary determination.
- Figure 26: Same as Figure 25, but for a South polar pass during high magnetic activity.
- Figure 27: Same as Figure 25, but for a North polar pass during low magnetic activity.
- Figure 28: Same as Figure 25, but for a South polar pass during low magnetic activity.
- Figure 29: Summary of the oval size for active and quiet magnetic conditions as determined from the poleward and equatorward boundaries in Figure 25-28. Cross-hatched areas denote the range over which the boundary is indeterminate.

NORTH POLE

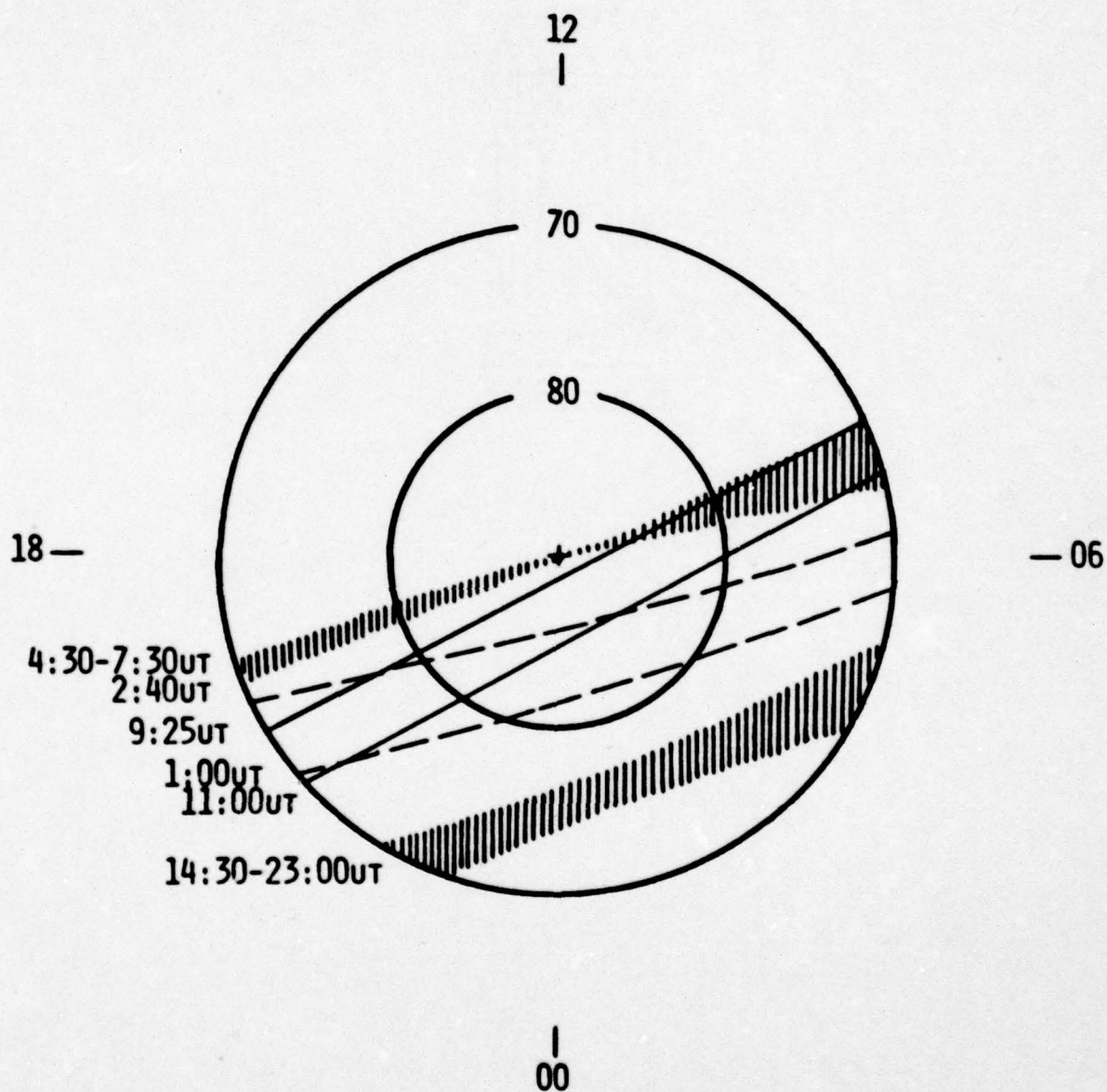
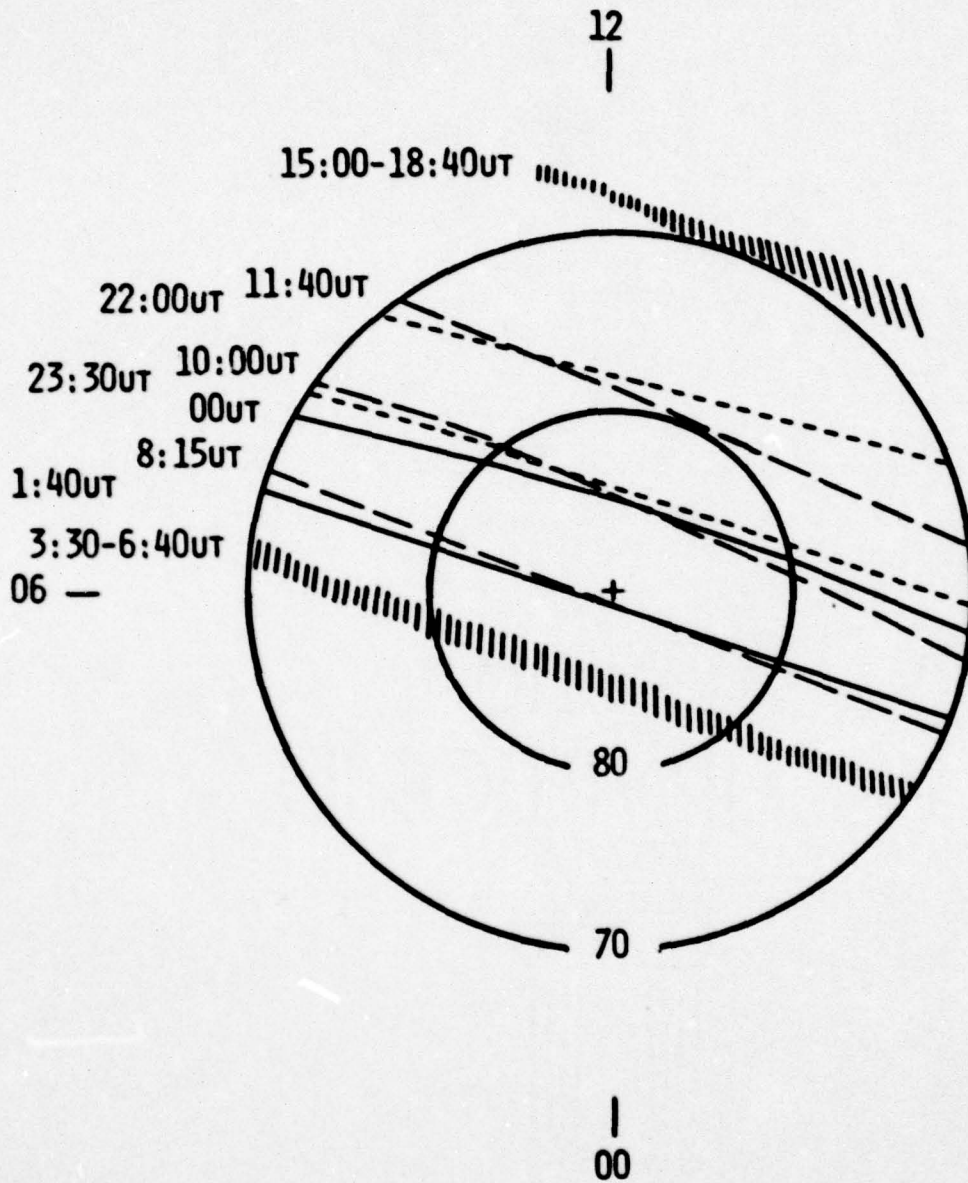


FIGURE 1

SOUTH POLE



— 18

FIGURE 2



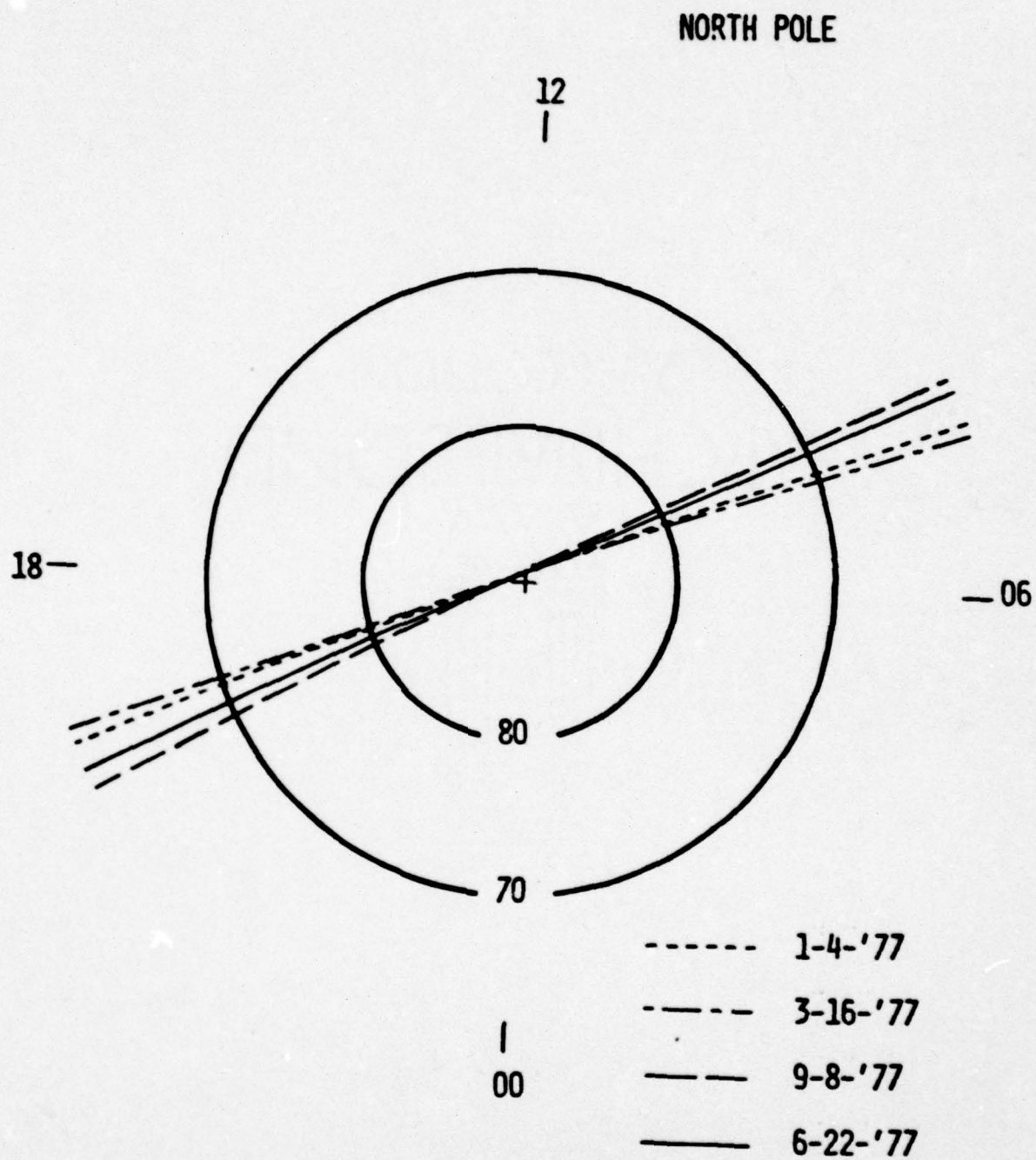


FIGURE 3

NORTH POLE

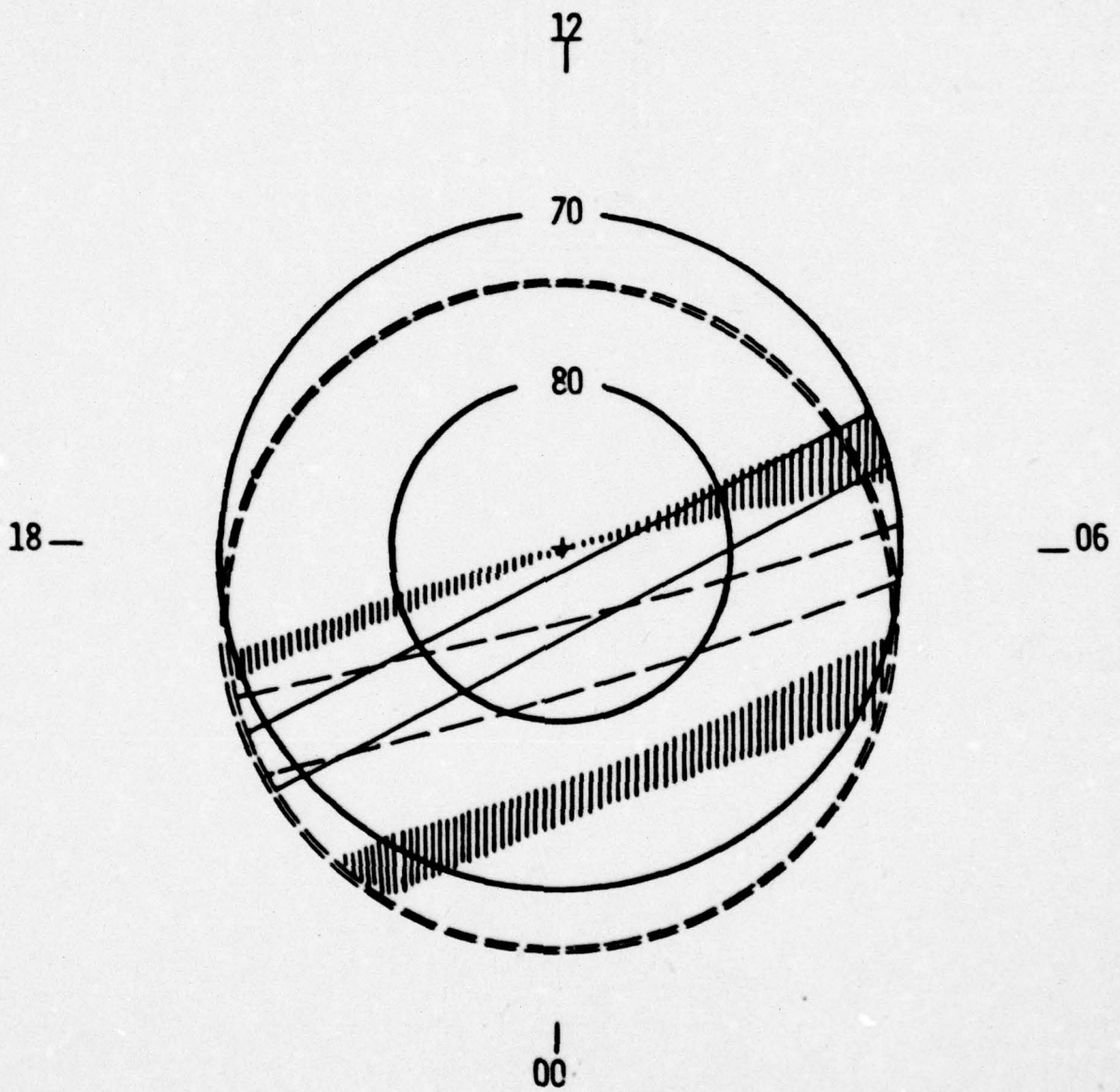


FIGURE 4

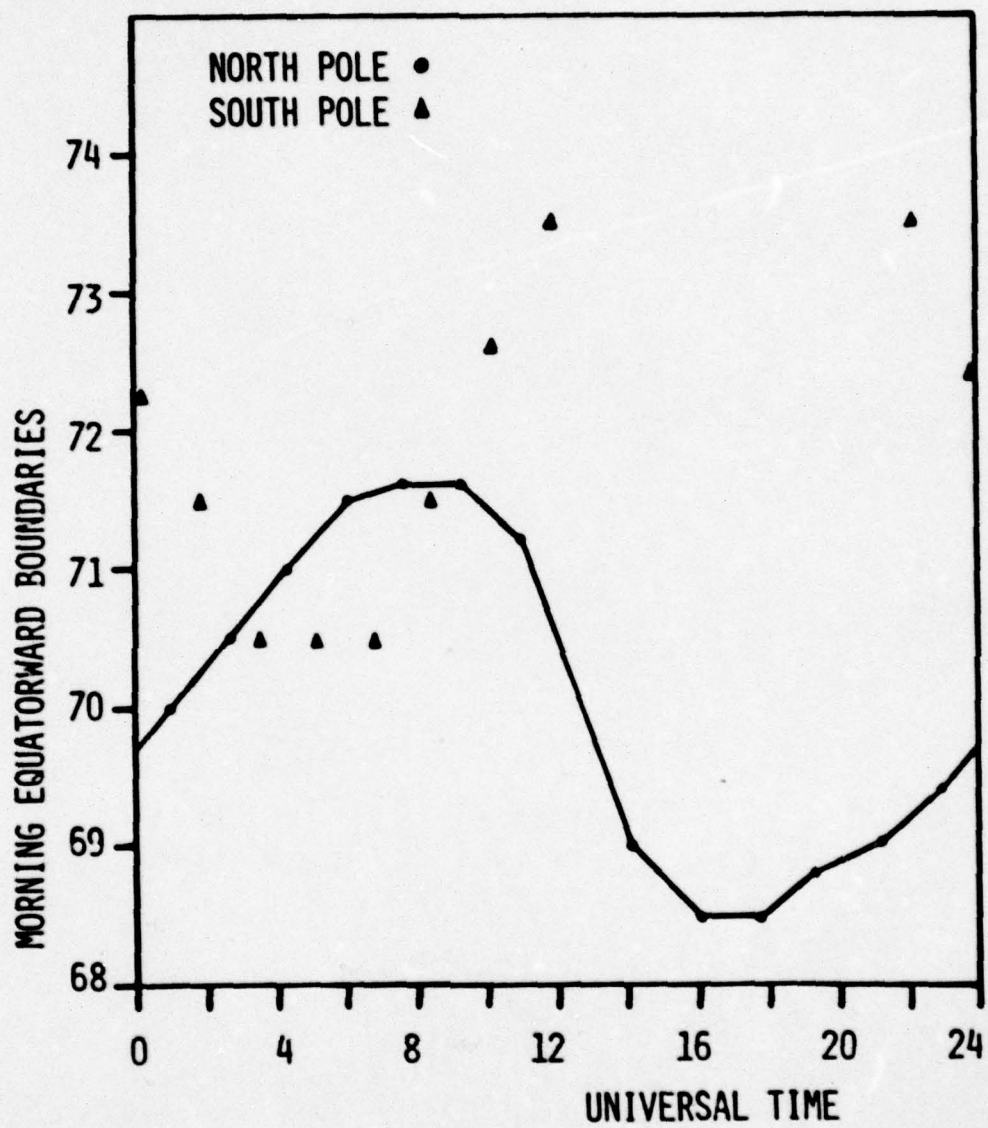


FIGURE 5



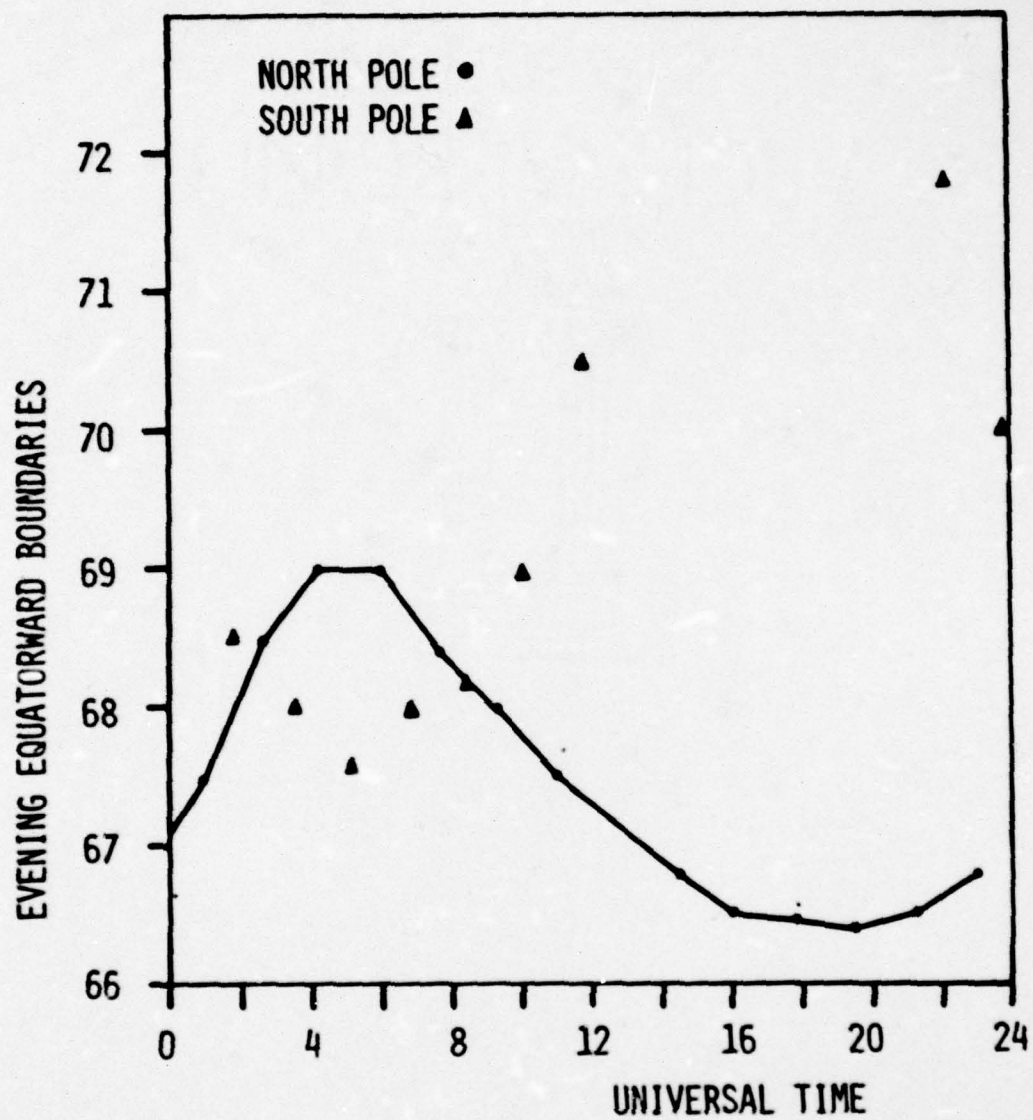


FIGURE 6

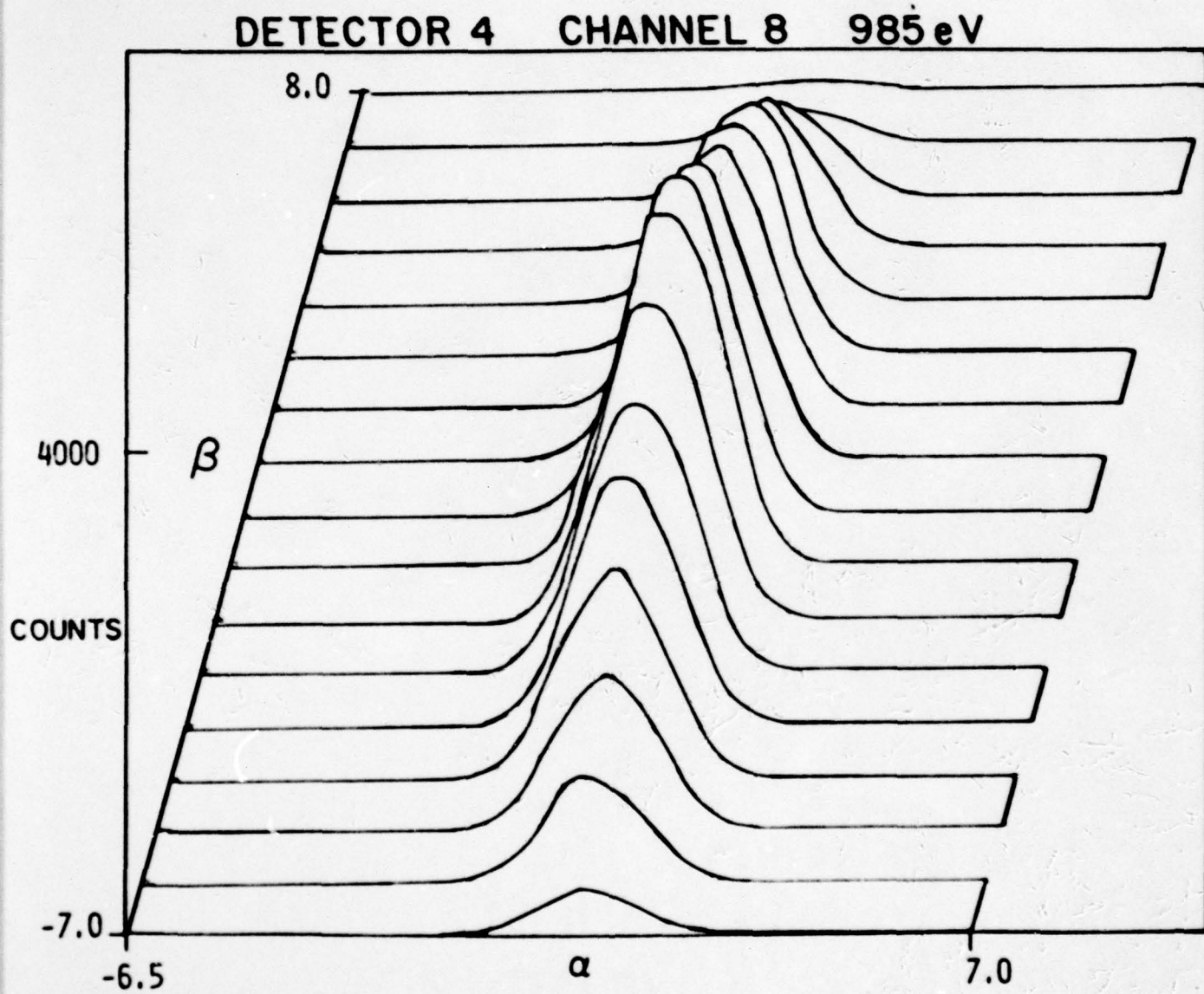


FIGURE 7

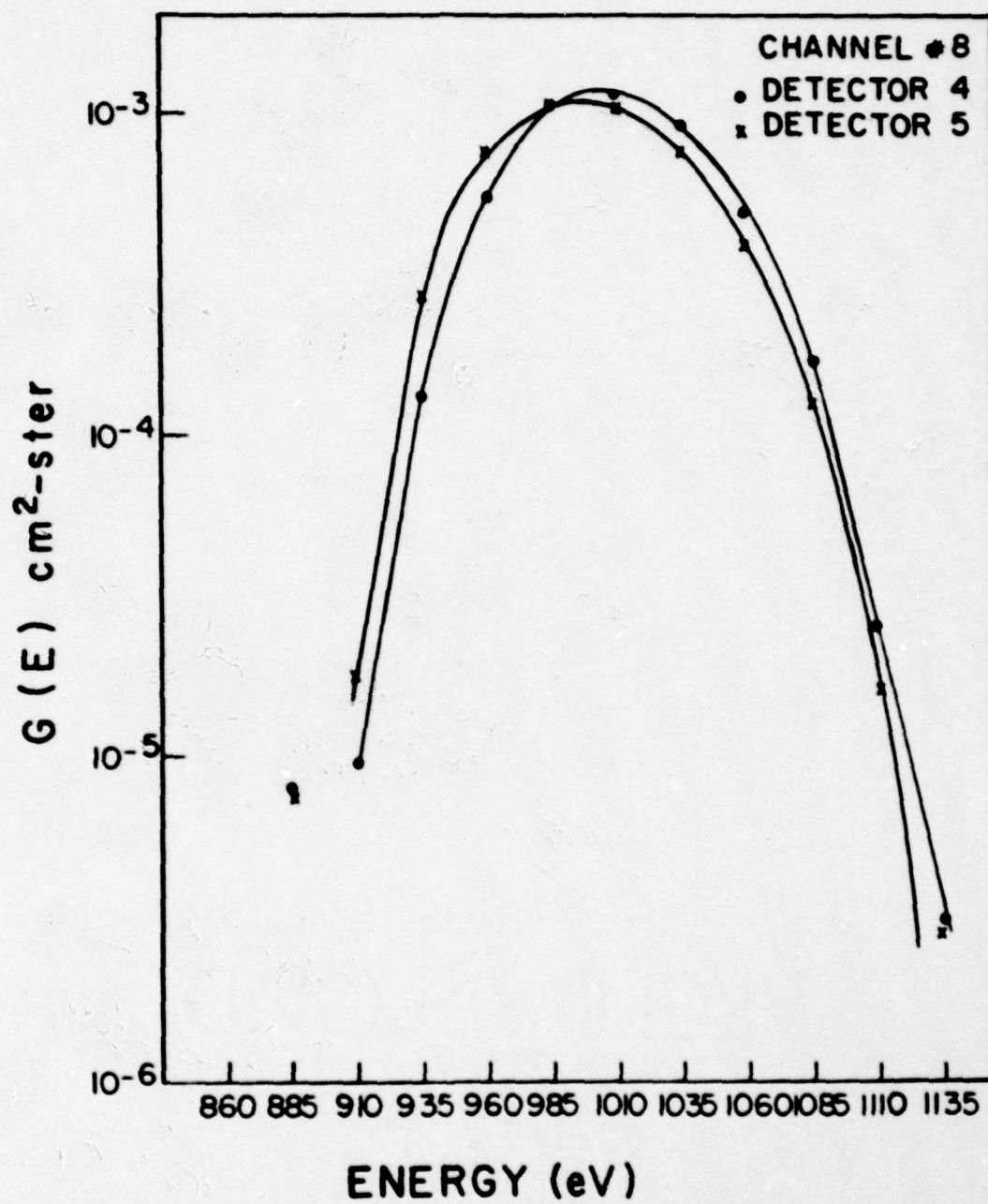


FIGURE 8A



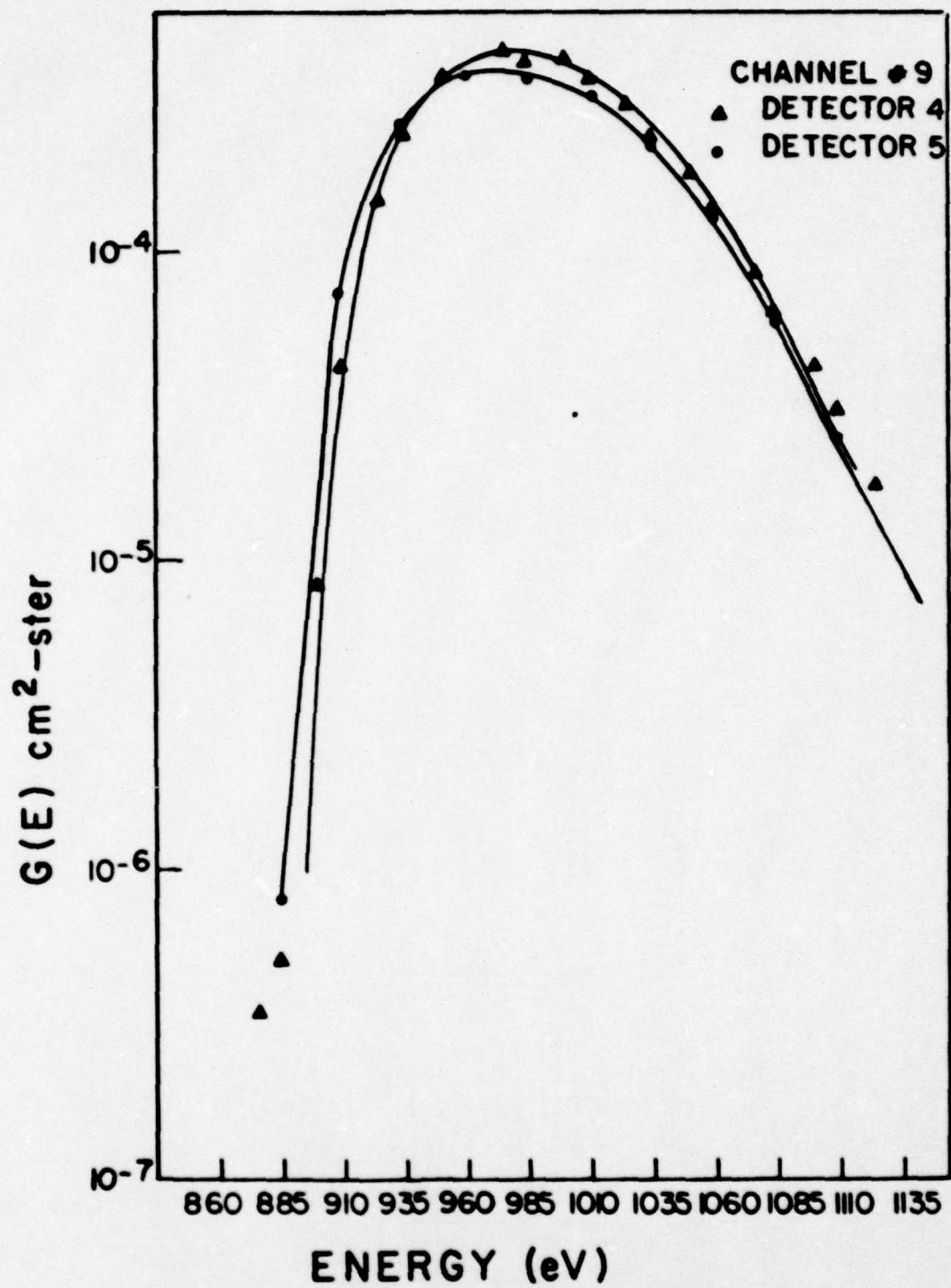


FIGURE 8B

# SSJ/3 ESA ASSEMBLY

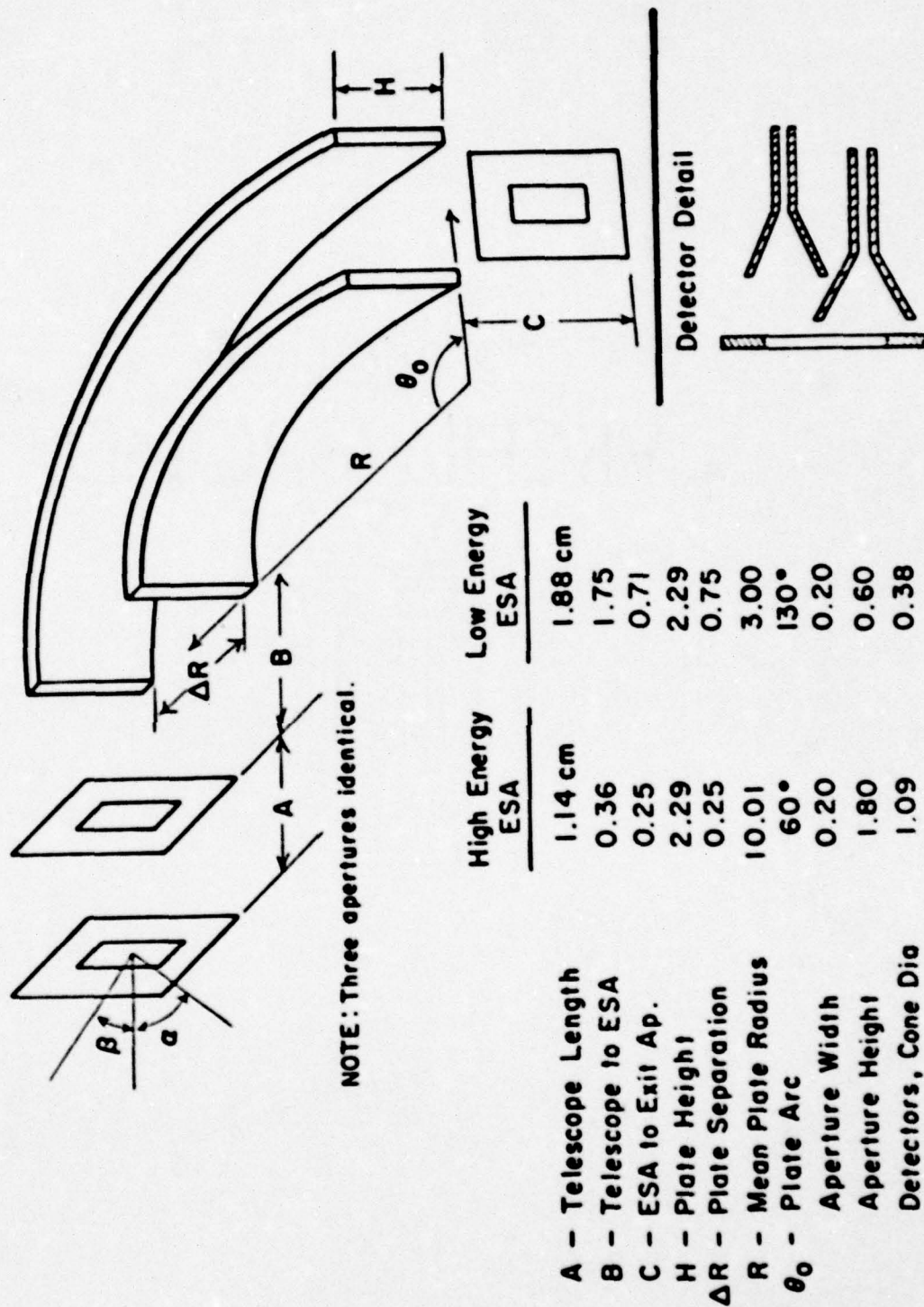


FIGURE 9

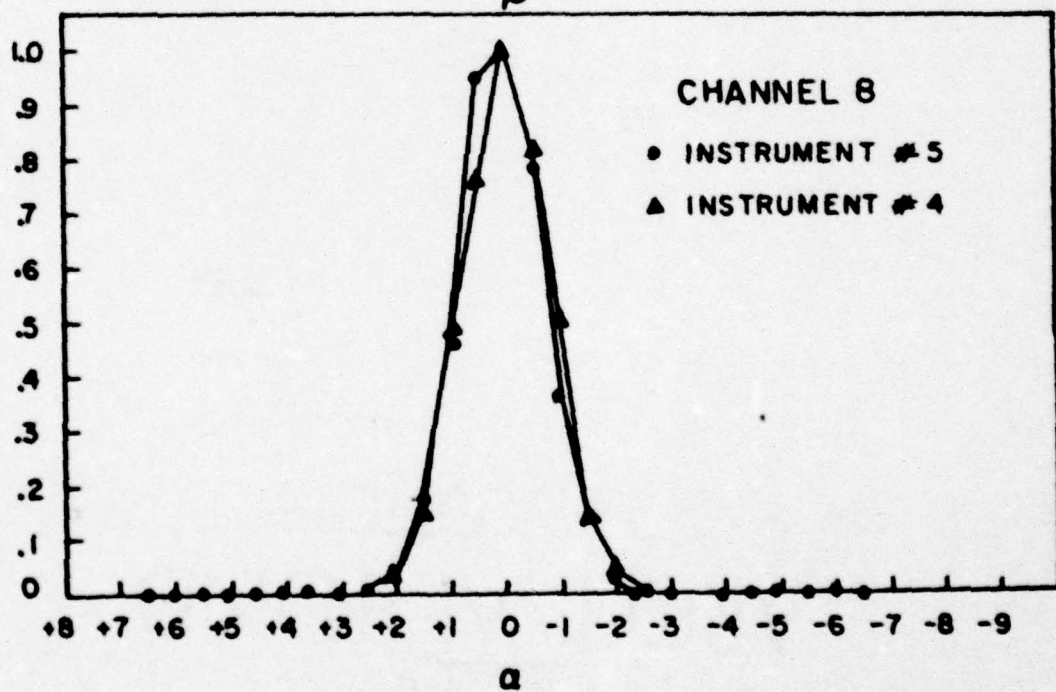
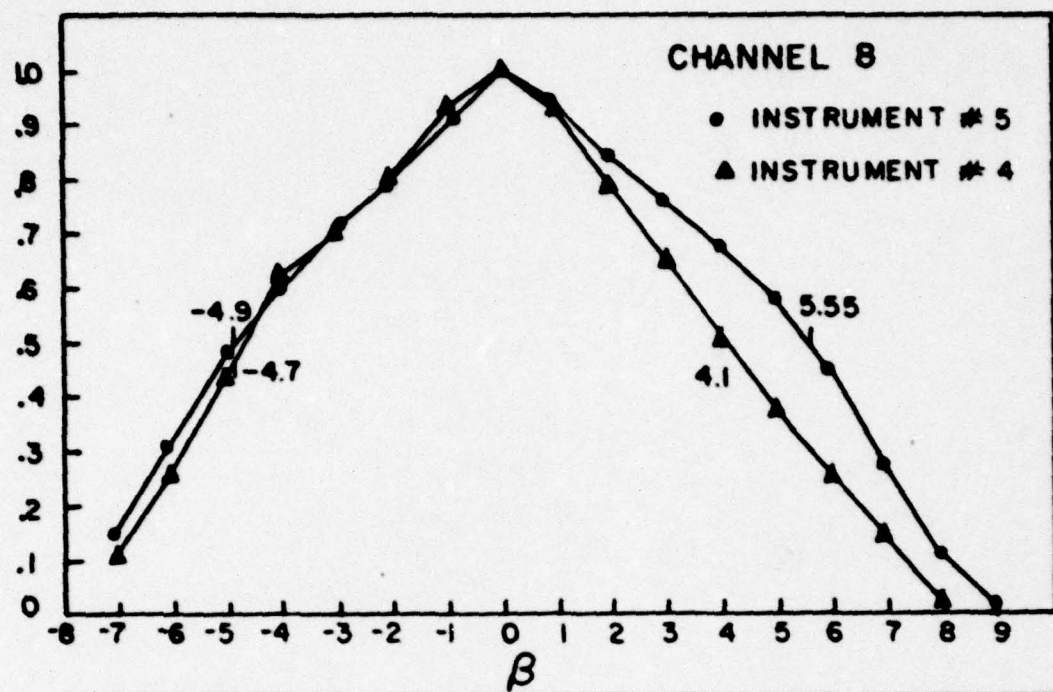


FIGURE 10



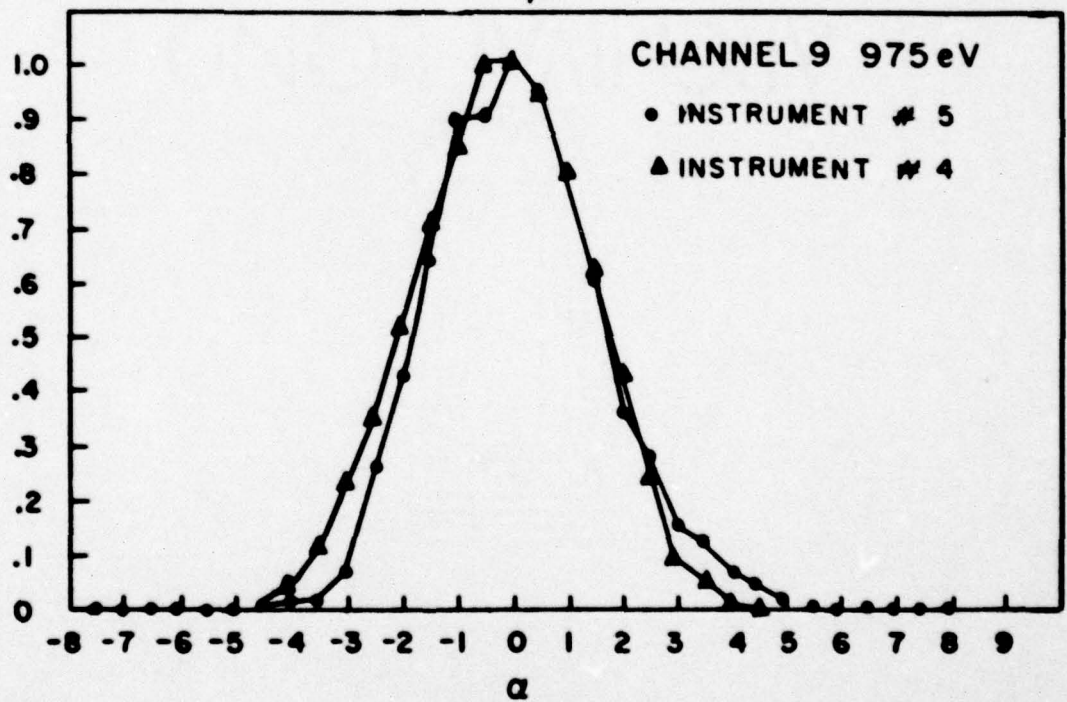
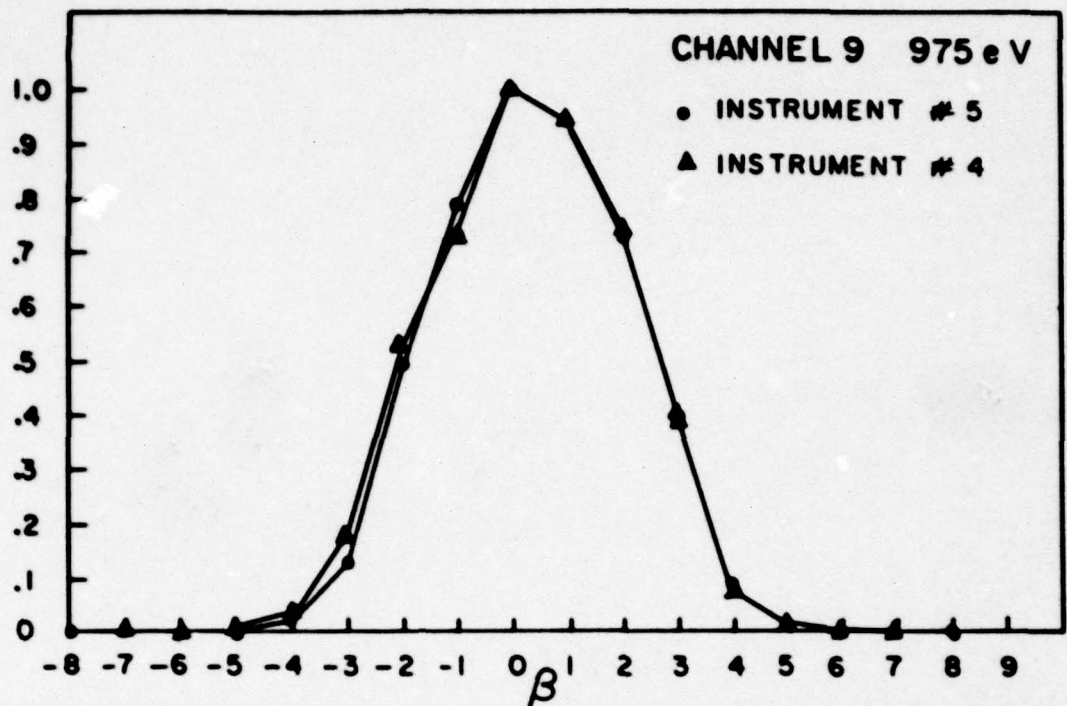


FIGURE 11

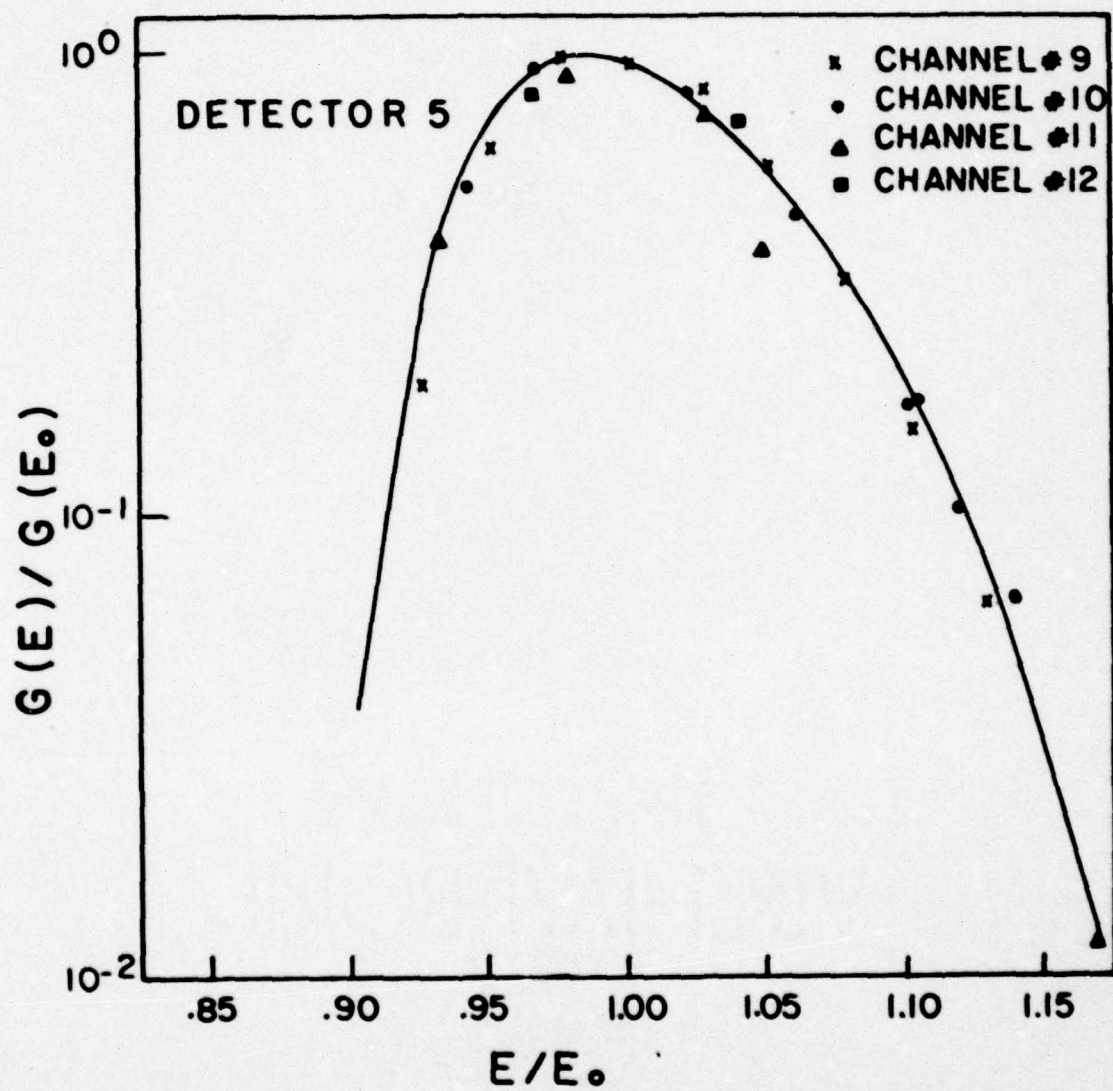


FIGURE 12

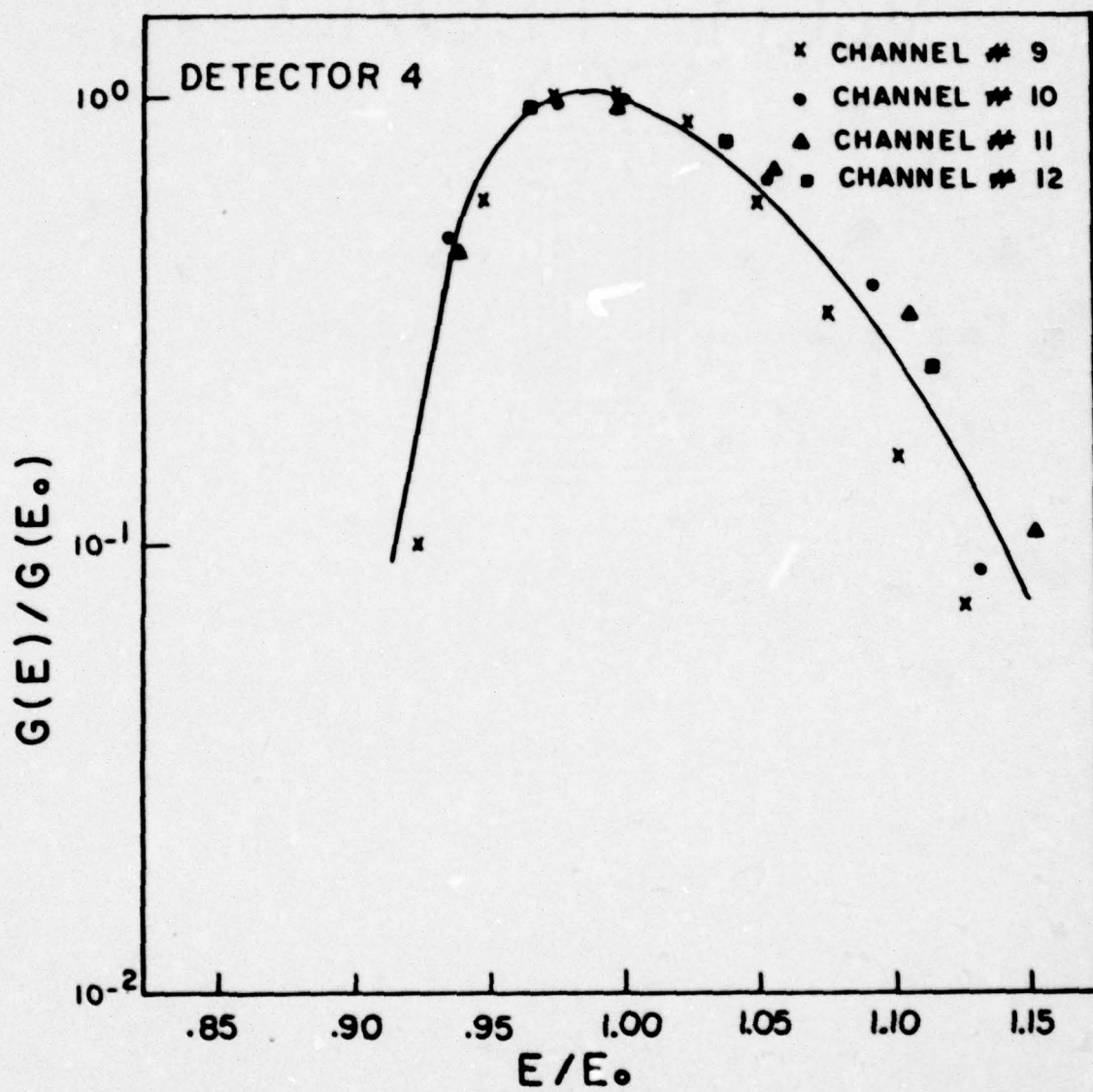


FIGURE 13



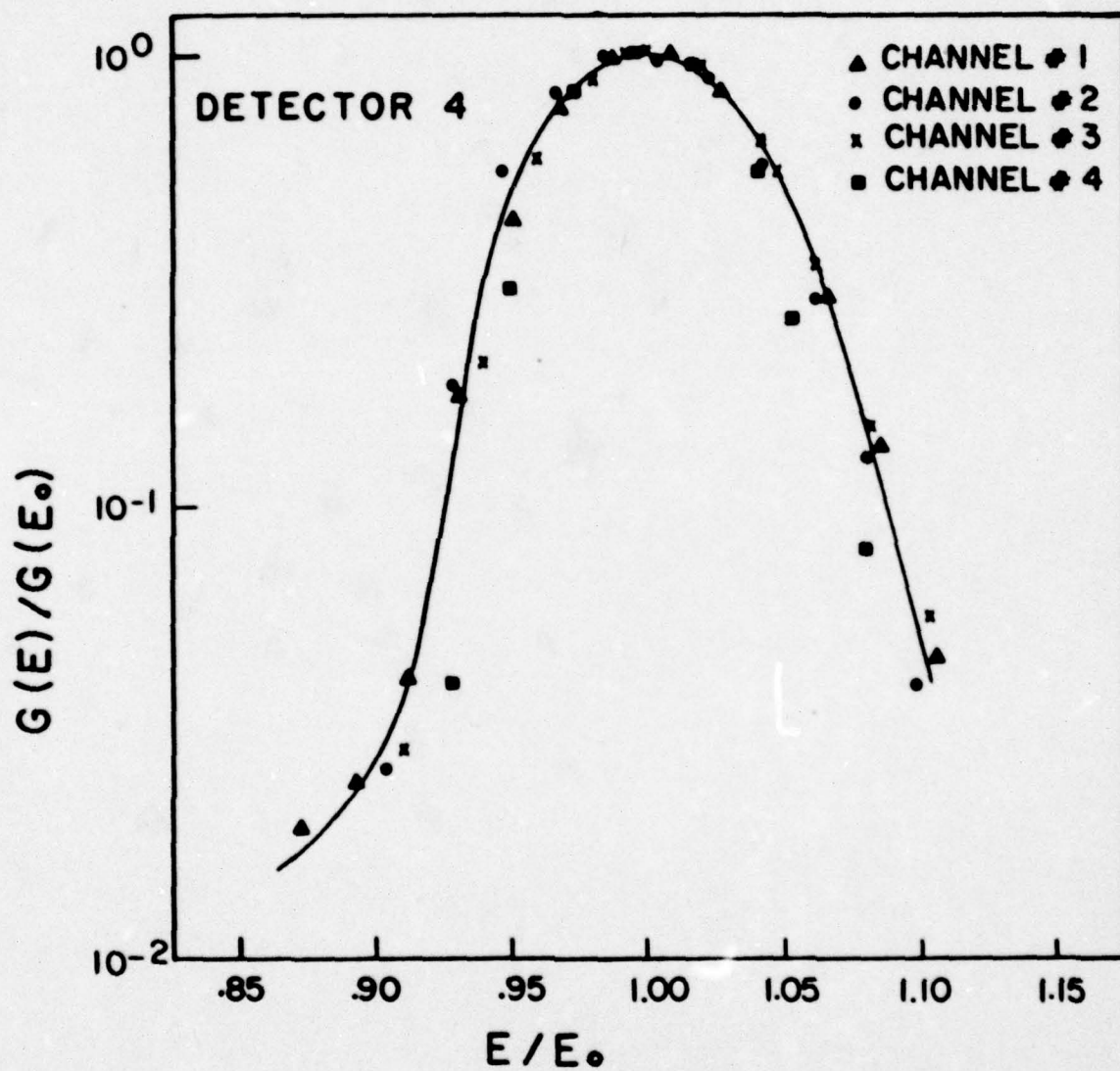


FIGURE 14

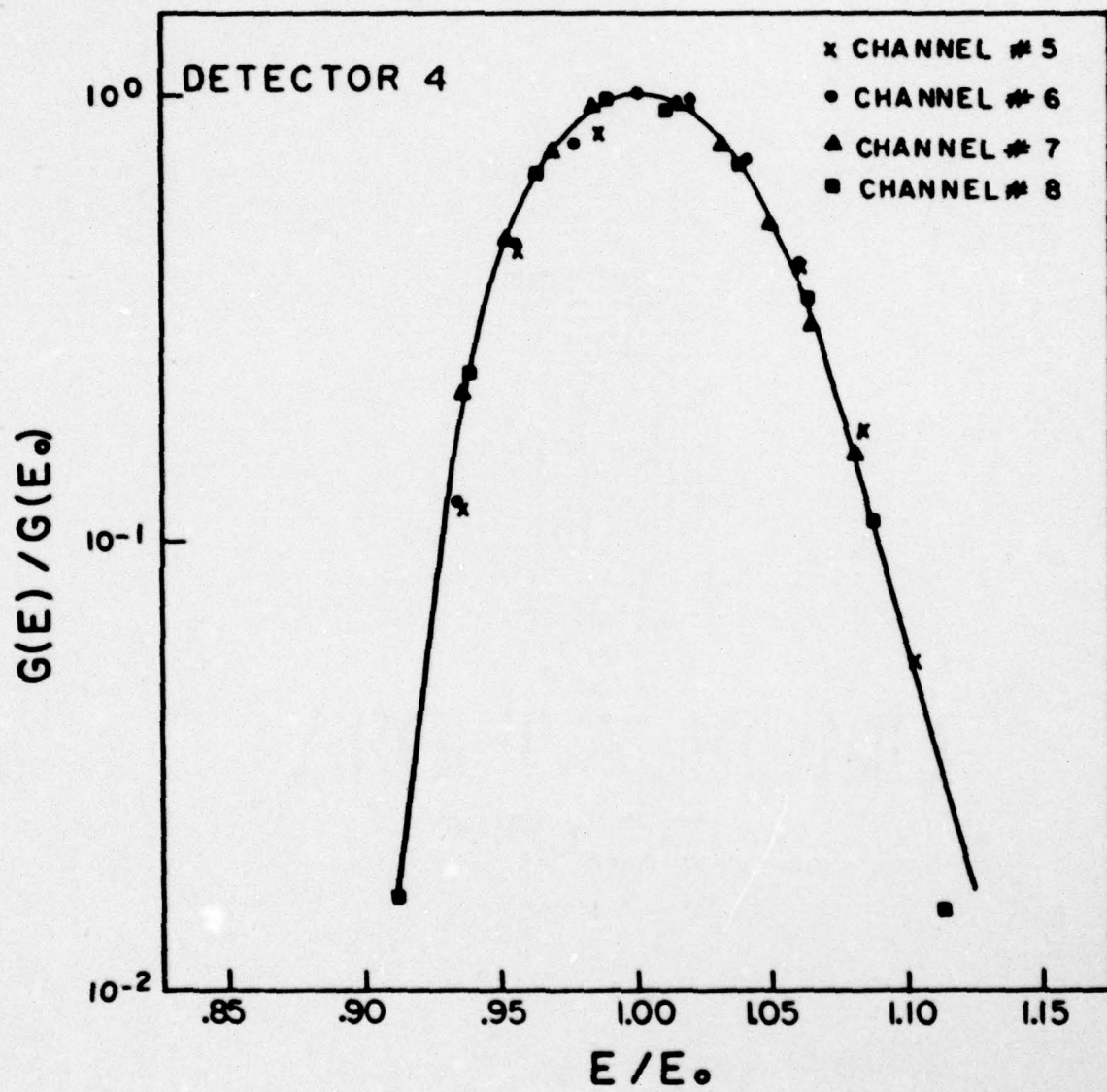


FIGURE 15

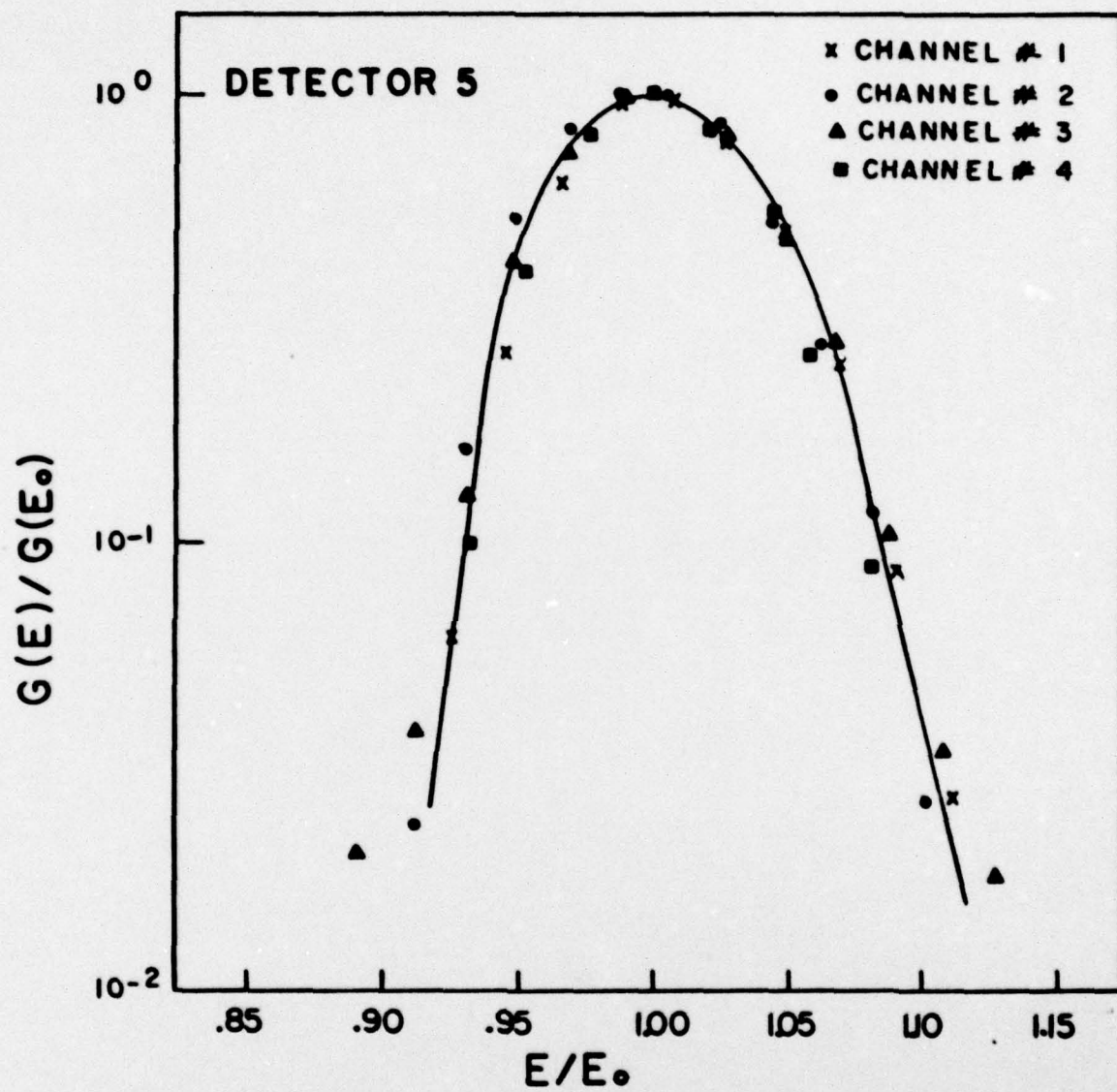


FIGURE 16



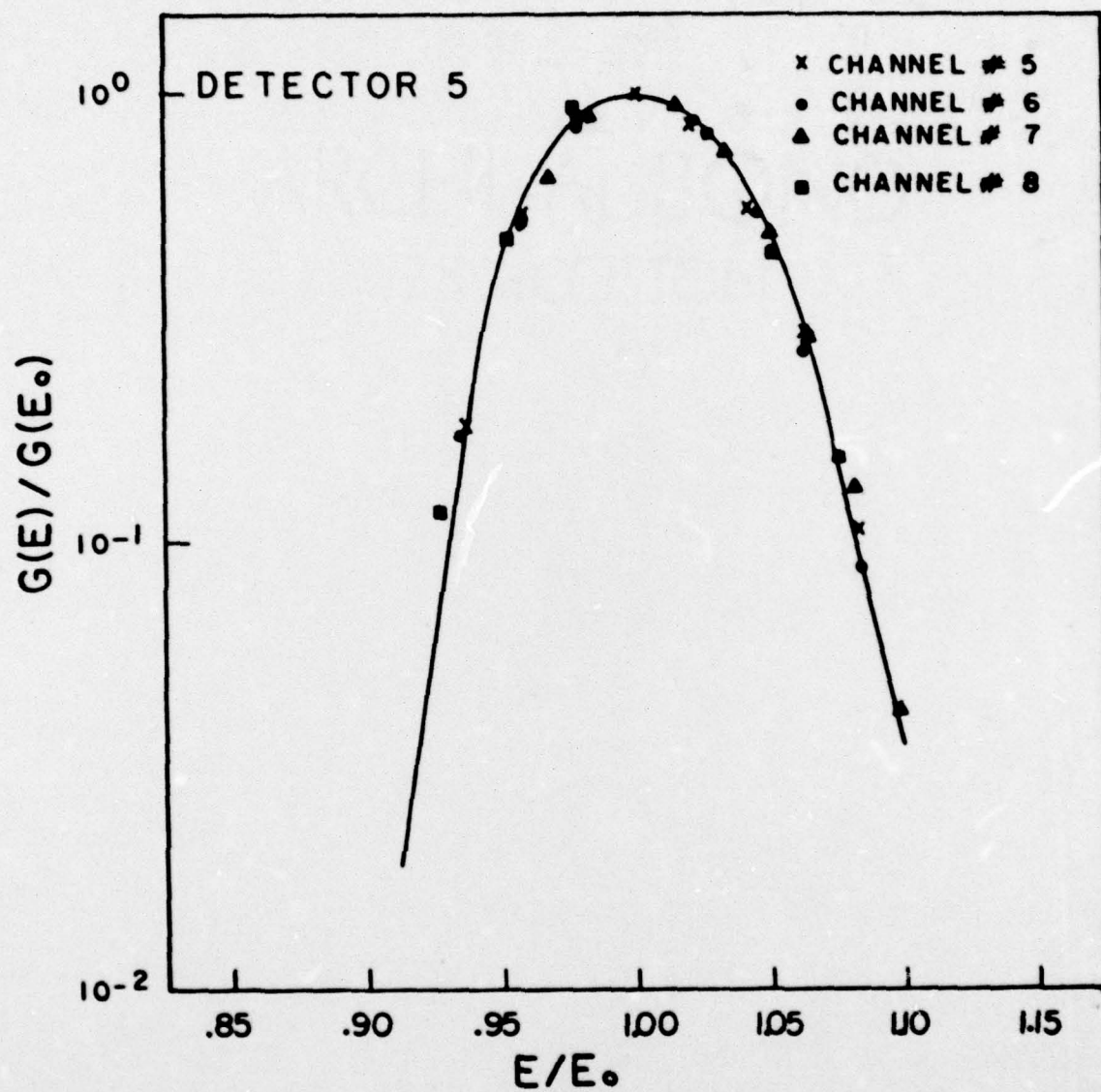


FIGURE 17

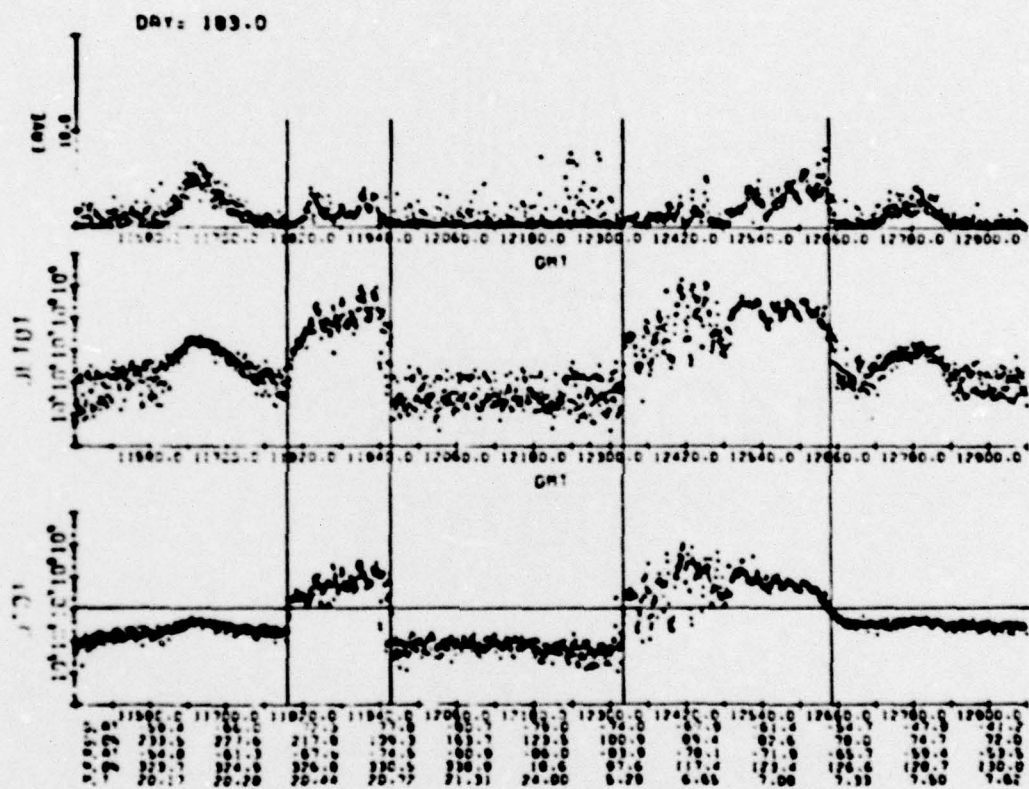


FIGURE 18

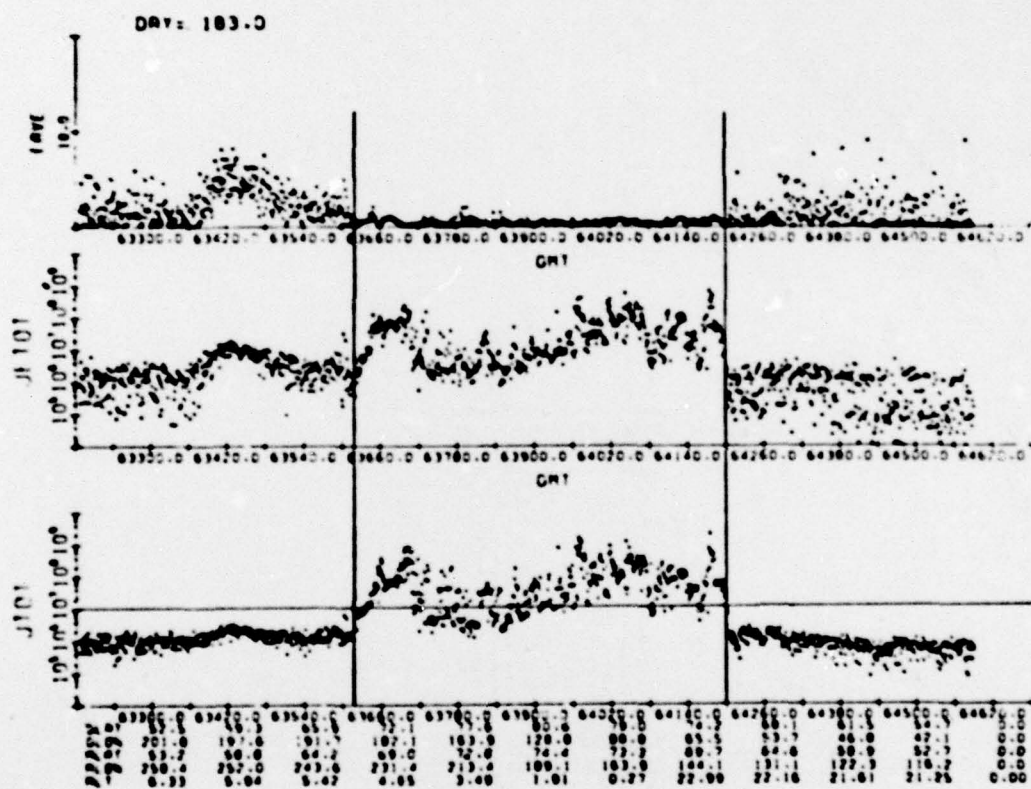


FIGURE 19



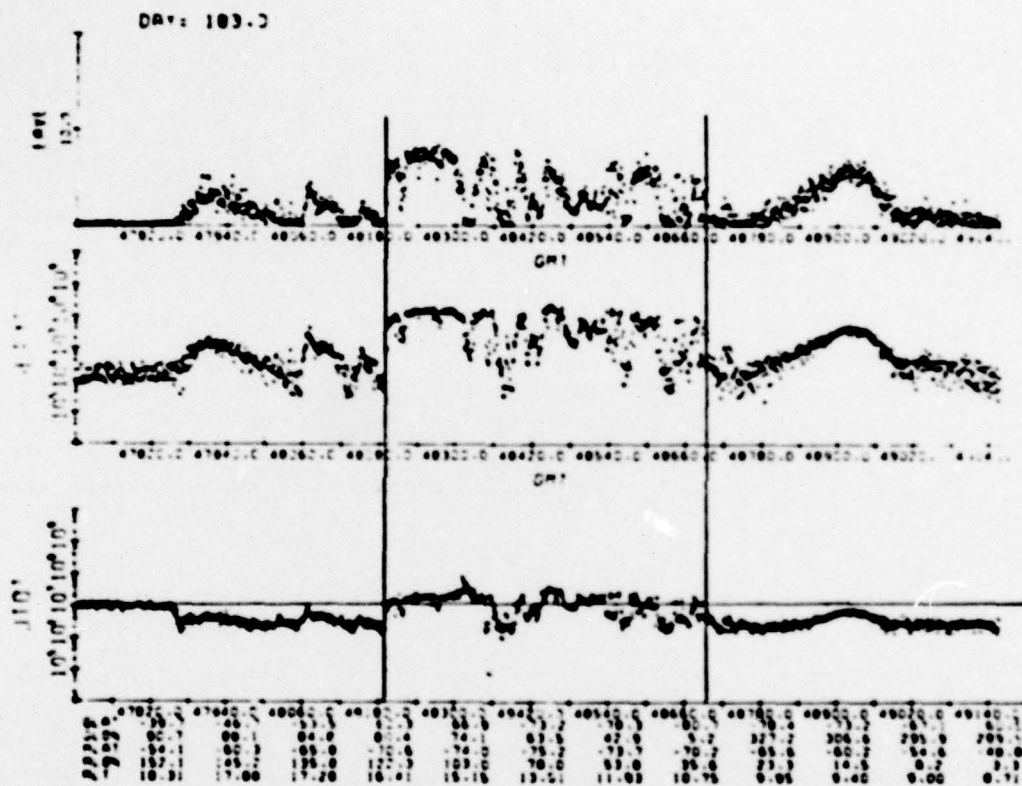


FIGURE 20

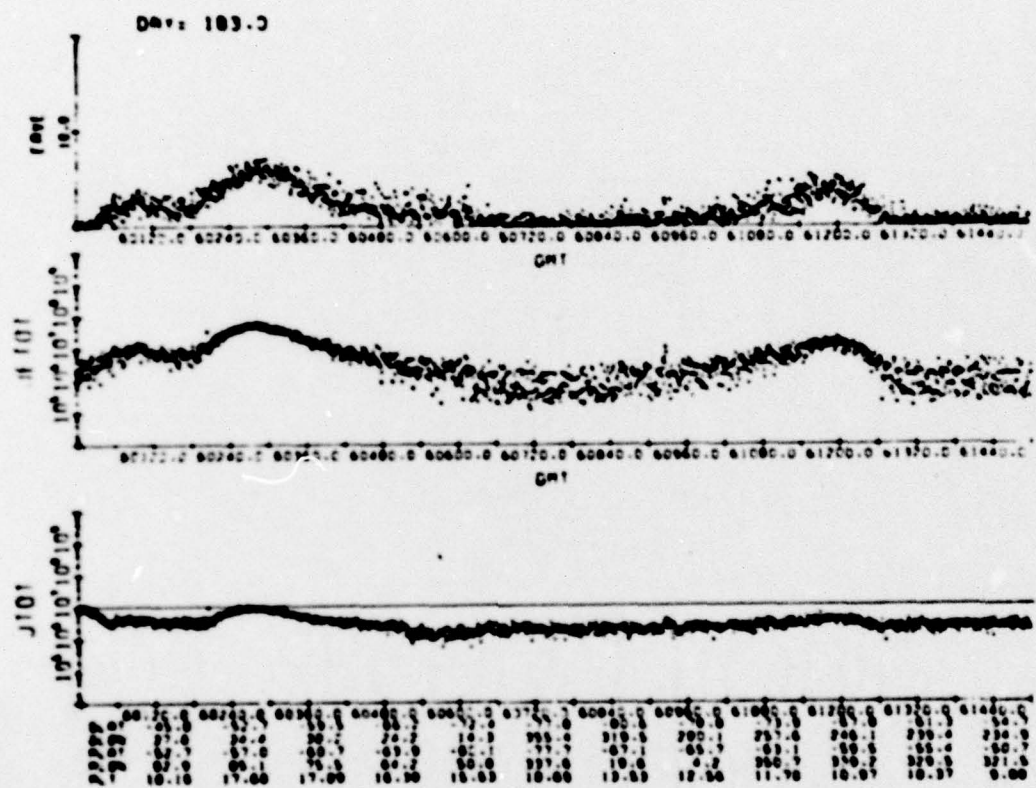


FIGURE 21

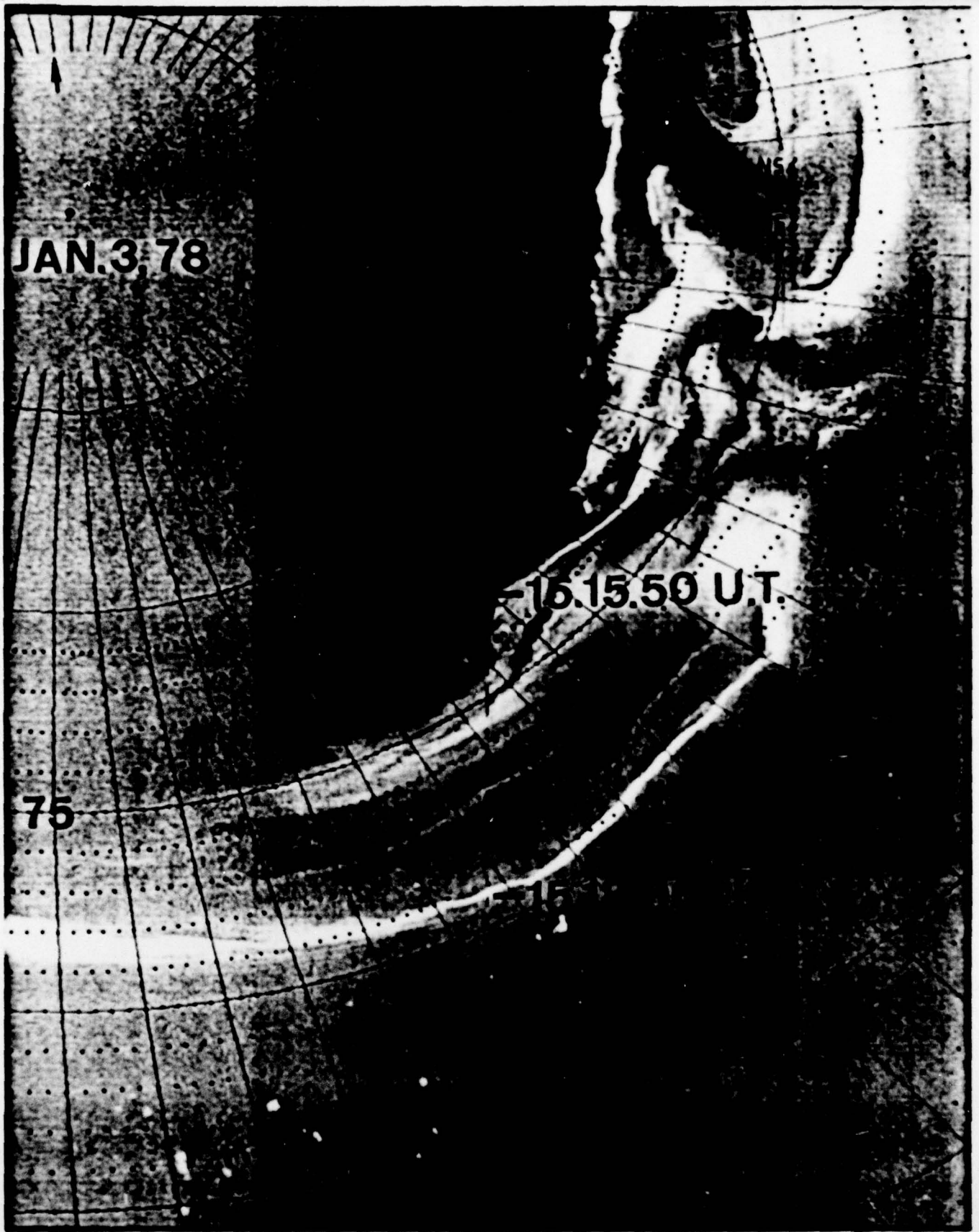


FIGURE 22



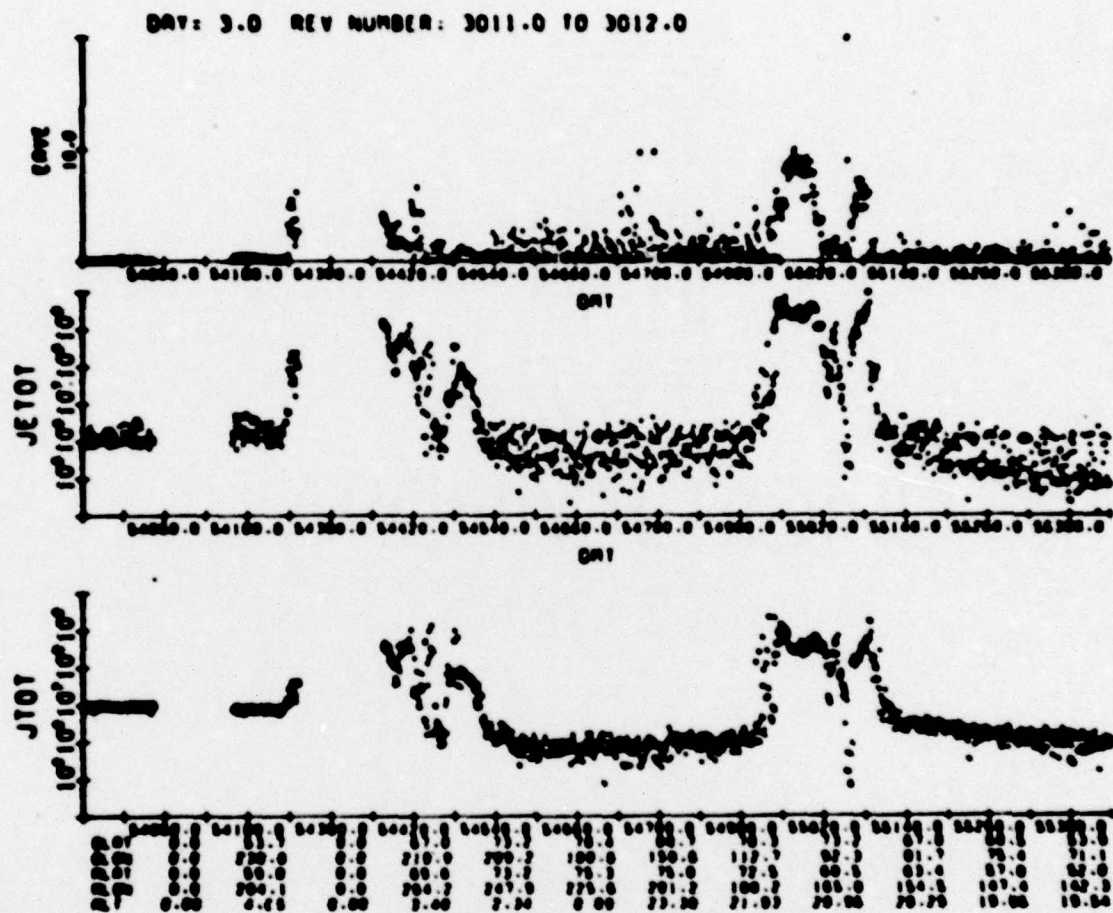


FIGURE 23

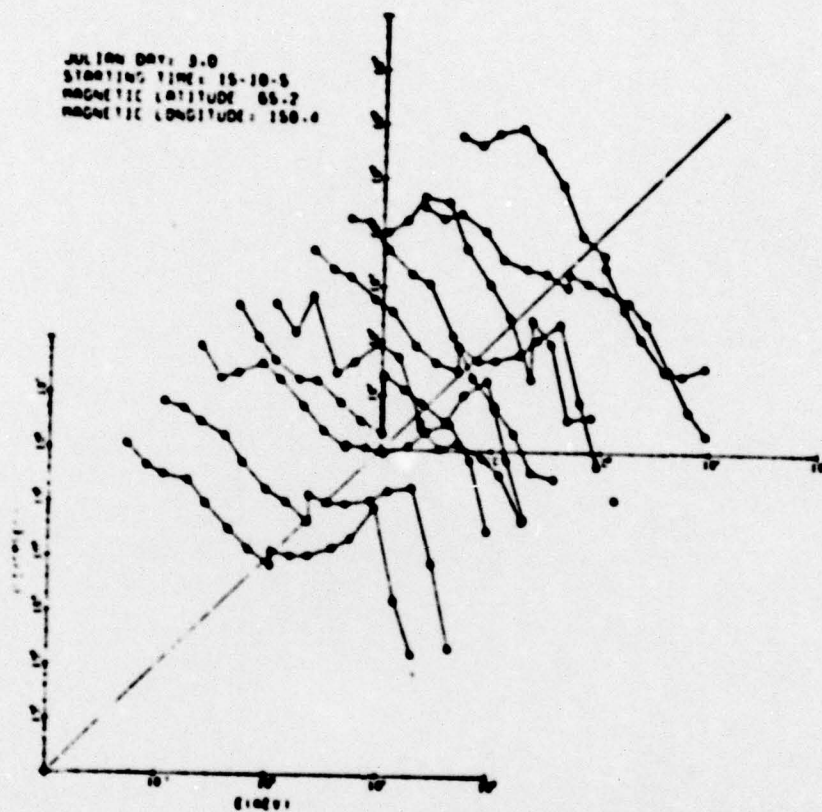


FIGURE 24

$K_p = 5+$

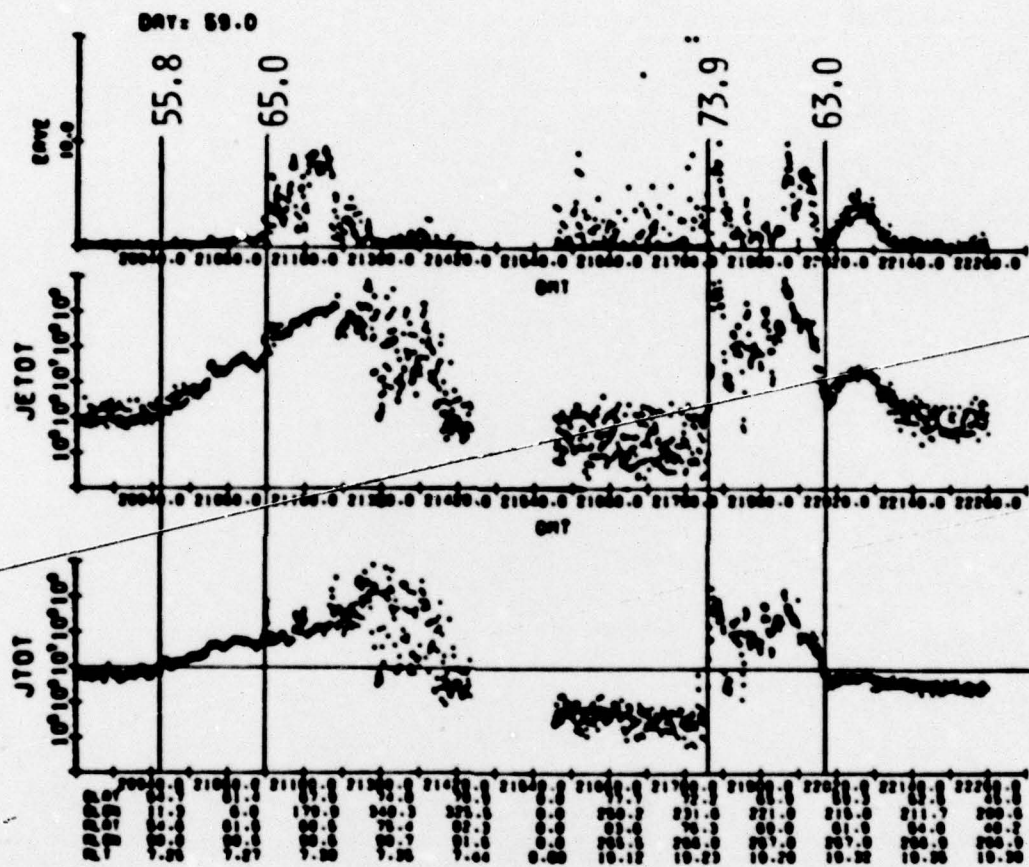


FIGURE 25



$K_p = 4+$

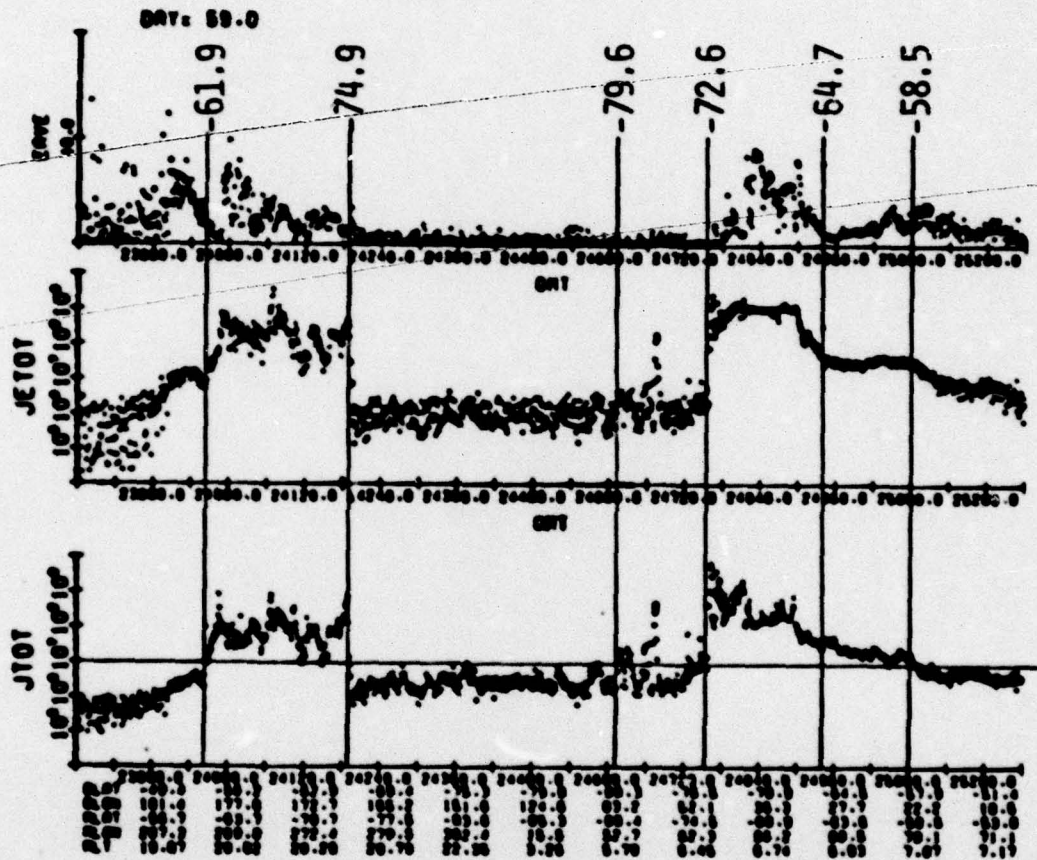


FIGURE 26

$$K_p = 0$$

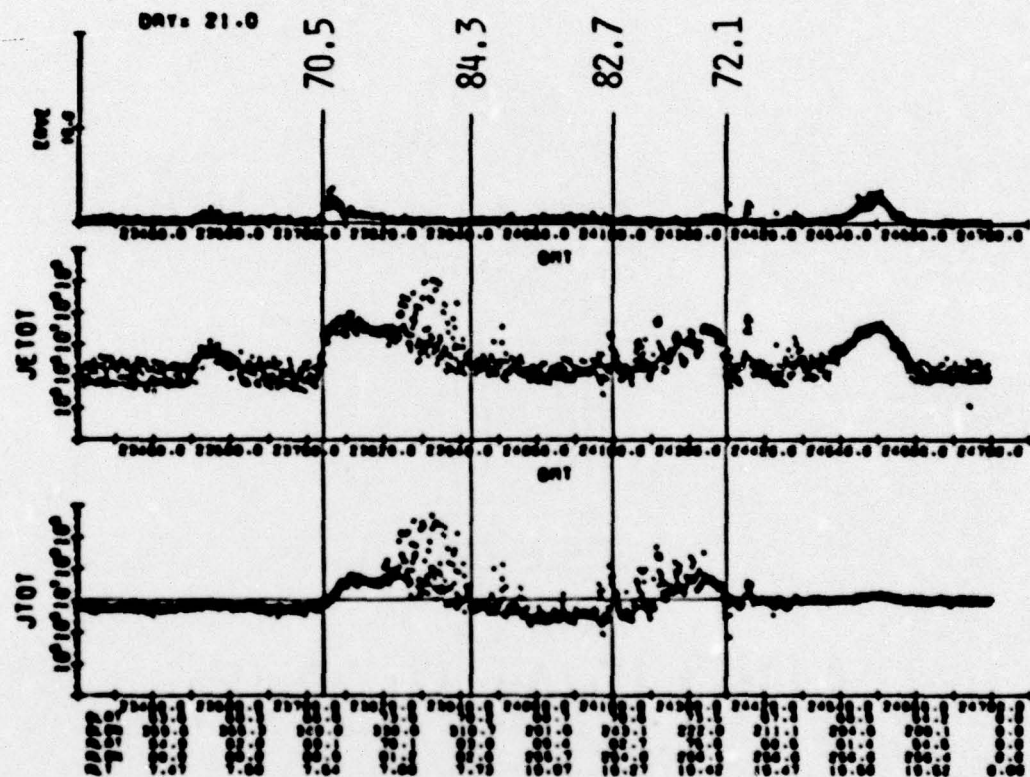


FIGURE 27



$K_p=0$

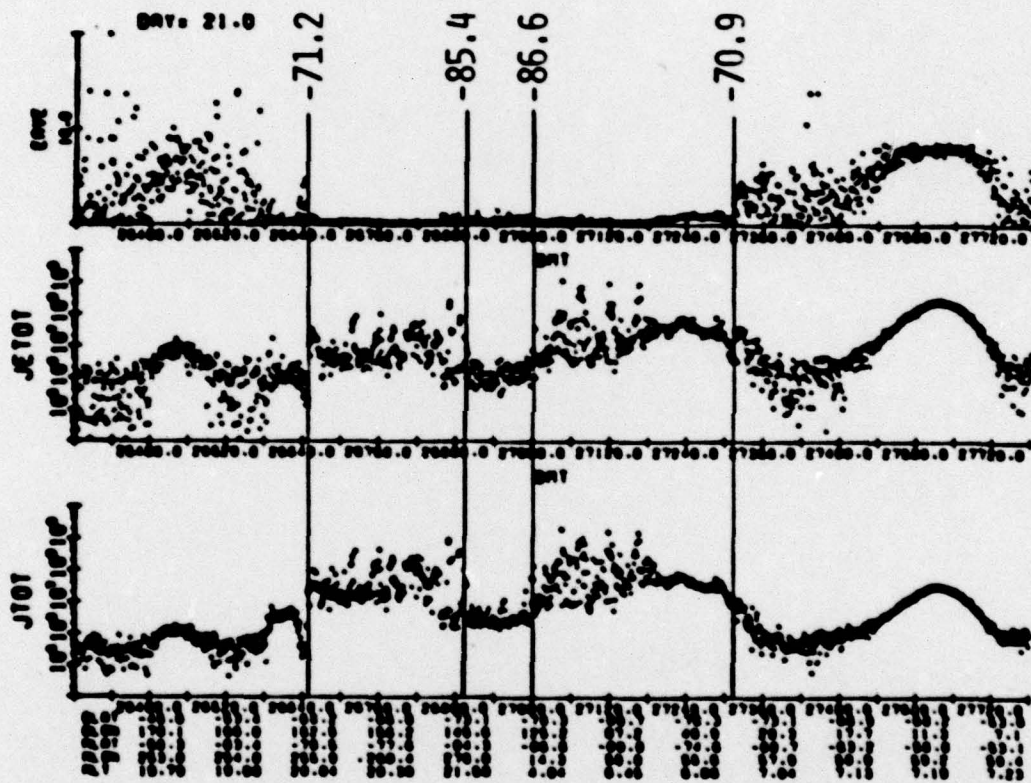


FIGURE 28



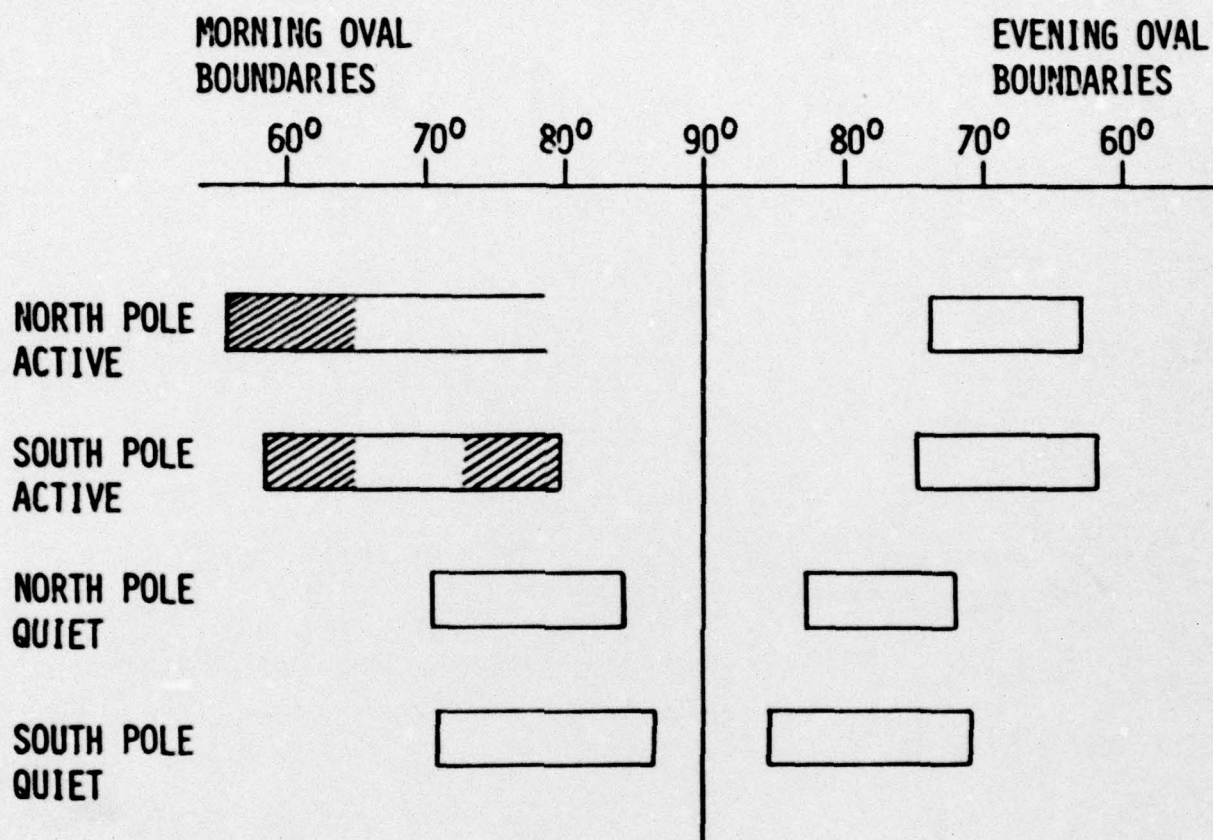


FIGURE 29